NEAR-FIELD INTER-COUPLED CELL-LESS METASURFACE FABRICS AND THEIR APPLICATIONS

A THESIS SUBMITTED TO

THE GRADUATE SCHOOL OF ENGINEERING AND SCIENCE

OF BILKENT UNIVERSITY

IN PARTIAL FULFILLMENT OF THE REQUIREMENTS FOR

THE DEGREE OF

MASTER OF SCIENCE

IN

ELECTRICAL AND ELECTRONICS ENGINEERING

By

Hüseyin Bilge Yağcı

July 2021

NEAR-FIELD INTER-COUPLED CELL-LESS METASURFACE FABRICS AND THEIR APPLICATIONS
By Hüseyin Bilge Yağcı
July 2021

We certify that we have read this thesis and that in our opinion it is fully adequate, in scope and in quality, as a thesis for the degree of Master of Science.

Hilmi Volkan Demir(Advisor)

Vakur Behçet Ertürk

Talha Erdem

Approved for the Graduate School of Engineering and Science:

Ezhan Karaşan
Director of the Graduate School

ABSTRACT

NEAR-FIELD INTER-COUPLED CELL-LESS METASURFACE FABRICS AND THEIR APPLICATIONS

Hüseyin Bilge Yağcı
M.S. in Electrical and Electronics Engineering
Advisor: Hilmi Volkan Demir
July 2021

Metasurfaces are subwavelength-thick artificial structures with engineered responses, designed to provide functionalities that do not exist in the natural domain. Their application areas are broad and vary in both functionality and operation regime. Across all functionalities and regimes, the fundamental purpose behind the metasurfaces is to manipulate the surrounding electromagnetic landscape to form devices with superior sensitivity and efficiency. With conventional design routines and available high-index materials, this was achieved across longer wavelengths in the past decade. However, the lack of suitable materials in the higher frequencies limit the design space for the mainstream approaches that discretize the phase surface with the help of independent nanostructures, dubbed as “meta-cells” or alternatively “meta-atoms”. With increasing frequencies, the discrepancy between a smoothly-changing effective index surface and a discretized step-index surface increase, resulting in unwanted scattering. Additionally, the methodology behind the uncoupled scatterers break up as the meta-atoms act collectively in sufficiently small scales, resulting in topology-induced errors in the generated phase response. In this thesis, a new class of highly efficient metasurfaces relying on the near-field coupling of identical scatterers in a continuous fabric is proposed. Contrary to the conventional approach, which sees the intercell coupling as phase distortions, our proposed methodology utilizes near-field coupling between the nearest neighbors, enabling lattice generation schemes applicable at broad scales that are insusceptible to topological errors. Owing to these, this methodology offers opportunities in further miniaturization of optical consumer products. One of the functionalities high in demand from metasurfaces is efficient and achromatic focusing with compact devices in the visible range, core to contact lenses and smartphone cameras. However, the examples in the literature are not sufficient in terms of either broadband performance or efficiency. Our proposed phase acquisition scheme effectively eliminates inhomogeneous scattering while reducing the design procedure to the tiling of the phase surface, subject to a function of the nearest-neighbor distances. Here, with this methodology, one cylindrical and one circular achromatic metasurface lenses (metalenses) with near-diffraction-limit focusing operating across the whole visible spectrum are demonstrated as a proof of concept. The validity of the utilized approach is confirmed via both waveguide solutions and full electromagnetic computations. Both structures proved to be highly efficient, with the cylindrical one having superior efficiency in its preferred polarization, whereas the circular one is highly efficient while operating independent of polarization. These findings prove the applicability of our near-field inter-coupled cell-less metasurface fabrics as a compact and efficient optical device generation framework.

Keywords: metasurface, metastructure, near-field coupling, field enhancement.

ÖZET

YAKIN-ALAN KOMŞU-BAĞLAŞIMLI HÜCRESİZ METAYÜZEY DOKU VE UYGULAMALARI

Hüseyin Bilge Yağcı
Elektrik ve Elektronik Mühendisliği, Yüksek Lisans
Tez Danışmanı: Hilmi Volkan Demir
Temmuz 2021

Metayüzeyler, doğal alanda mevcut olmayan, isteğe bağlı işlevsellikleri gerçeklemek için tasarlanmış, dalgaboyu-altı kalınlığında yapay yapılardır. Hem işlevsellik hem de çalışma aralıkları bakımından farklılık gösterebilirler ve buna dayalı olarak geniş bir uygulama alanında tasarlanmaya elverişlidirler. İşlevsellikleri ve çalışma aralıkları fark etmeksizin metayüzeylerin arkasındaki temel amaç, üstün hassasiyet ve verimliliğe sahip cihazlar oluşturmak için çevreleyen elektromanyetik manzarayı işlemektir. Geleneksel tasarım rutinleri ve mevcut yüksek indeksli malzemelerle bu, geçtiğimiz on yılda uzun dalgaboyu limitinde elde edilmiştir. Bununla birlikte, daha yüksek frekanslarda uygun özelliklere sahip doğal malzemelerin olmaması, talep edilen faz cephesinin birbirinden bağımsız olarak oluşturulmuş "meta-hücreler" veya alternatif olarak "meta-atomlar" olarak adlandırılan nanoyapılar tarafından örneklenmesini prensip edinmiş ana akım yaklaşımlar için tasarım alanını sınırlar. Artan frekanslarla, ideal olarak ulaşılmaya çalışılan kesintisiz-değişimli etkin kırıcılık indisi yüzeyi ile ayrık noktalarda örneklenmiş basamaklı-değişen indis yüzeyi arasındaki tutarsızlık artar ve istenmeyen saçılmalara sebebiyet verir. Ek olarak, tasarımlarda kullanılan ölçeklerin küçülmesi ile, istenen yüzeylerin oluşumu için kullanılan meta-atomların birbirlerinden bağımsız cevaplara sahip olmasına dayanan tasarım yöntemleri geçerliliklerini kaybetmekte ve üretilen faz yüzeylerinde oluşan örgüsel kaynaklı hatalar giderilememektedir. Bu tezde, yeni bir metayüzey sınıfı olarak kesintisiz bir doku olarak tasarlanmış özdeş saçıcıların yakın alan bağlaşımına dayanan yüksek verimli meta-yüzeyler önerilmiştir. Hücreler arası etkileşmeleri faz bozunumu olarak gören geleneksel yaklaşımın aksine, önerdiğimiz metodoloji en yakın komşular arasında yakın alan bağlaşımını kullanır ve topolojik hatalara karşı duyarsız, geniş ölçeklerde uygulanabilir örgü oluşturma şemalarını mümkün kılar. Bu özellikleri sayesinde, önerdiğimiz metodoloji optik tüketim ürünlerinin daha da küçültülmesine yönelik fırsatlar sunar. Kontakt lens ve akıllı telefon kameraları gibi ticarileştirmeye yatkın alanlarda yüksek talep gören ve meta-yüzeylerle yaratılmaya çalışılan işlevlerden biri, görünür dalgaboylarında verimli ve akromatik odaklamadır. Ancak literatürdeki örnekler ne geniş bant performansı ne de verimlilik açısından yeterli değildir. Önerdiğimiz faz edinim yaklaşımımız homojen olmayan saçılmaları etkin bir şekilde ortadan kaldırırken, istenilen işlevselliğin tasarım prosedürünü, kesintisiz bir dokudaki yakın-komşu uzaklıklarını gereken faz yüzeyine göre belirlemeye indirgemektedir. Burada, önerdiğimiz metodoloji ile tasarladığımız, tüm görünür spektrum boyunca çalışan, kırınım-sınırına-yakın odaklanmaya sahip bir silindirik ve bir dairesel akromatik metayüzey lens (metalens), örnek uygulama ve yaklaşımın geçerliliğinin kanıtı olarak ortaya çıkarılmıştır. Kullanılan yaklaşımın geçerliliği hem dalga kılavuzu çözümleri hem de tam elektromanyetik hesaplamalar ile doğrulanmıştır. Tasarlanan iki yapının da üstün verimliğe sahip oldukları görülürken, dairesel metalensimiz polarizasyondan bağımsız bir şekilde, silindirik metalens tasarımımız ise tasarım polarizasyonunda artırılmış olarak üstün verimliliğe sahiptir. Bu bulgular, yakın-alan komşu-bağlaşımlı hücresiz metayüzey dokularımızın bir küçültülmüş ve verimli optik cihaz oluşturma taslağı olarak uygulanabilirliğini kanıtlamaktadır.

Anahtar sözcükler: metayüzey, metayapı, yakın-alan bağlaşımı, alan kuvvetlendirme.

Acknowledgement

First and foremost, I thank my advisor Prof. Hilmi Volkan Demir. Before joining his group, I was a graduate student without a clear target, a working methodology or sufficient self-confidence. He believed in me when I did not believe in myself and guided me academically during my studies. I am forever indebted to him.

I want to thank Prof. Vakur B. Ertürk and Asst. Prof. Talha Erdem for accepting to be on my thesis jury.

I would like to thank Dr. Savaş Delikanlı, Assoc. Prof. Betül Canımkurbey, Dr. Volodymyr Sheremet, and Dr. Nina Sheremet for their eagerness to impart wisdom. They had to try numerous times to overcome my thick skull. Special thanks to Dr. Negar Gheshlaghi for her interest in my potential and her kind soul.

I thank all my fellow group members, with whom I have shared countless conversations and ideas. With all good and bad things, each of them have a special place in my heart.

I thank my mother Ayşe for bearing with me when I was stressed out, and her inability to stop thinking about my well-being. I am going to need a lot of those.

Lastly, I thank my spouse Ecehan for accepting me as I am and her never-ending support.

Contents

List of Figures

List of Tables

Chapter 1

Introduction

Light is the cornerstone of our lives. Primates and mankind are among the most capable species in the animal kingdom when it comes to vision [3, 4] - arguably as a consequence of co-evolution with venomous snakes [5]. Unsurprisingly, optics has been the difference maker in the advance of humankind, as a key driving force of technology and a propagator of exploration on our world simultaneously. Optics brought the ability to navigate in the seas, observe faraway galaxies and broadband global communication. The consumer products also benefited from these advancements: spectacles, portable cameras and CD/DVD memory are among the most influential optical inventions. The last decade saw the widespread use of smartphones and Internet of Things (IoT) - an exponential increase in portable sensors that can see, hear, compute, and communicate across the globe. This was made possible with scaling of electronic components in accordance with Moore's law, as well as the availability of small-scale sensors.

The optical components, in a general sense, are information-processing elements. Light having a certain wavelength (energy), direction and polarization enters an optical component, and leaves with some alterations. Linear optical components such as polarizers, beamsplitters, lenses and birefringent crystals transform the three fundamental properties of the incoming light and/or modulate its total intensity. With the aid of these, optical setups with lenses and masks enabled the civilization to calculate Fourier-domain representations and perform advanced filtering before the advent of modern computational tools.

With the advancement in fabrication processes, there has been an increasing incentive to miniaturize the optical components and adjust their manufacturing processes to be compatible with the silicon industry, which resulted in much more compact, low-cost and accessible optical components. This is due to scalable nature of processing technology. The miniaturization of optical devices (alongside an already-miniaturized micro-electro-mechanical systems) also contributed to the development of biomedical devices and fiber communication components; surgical lasers and optical communication technologies would not have been implemented without miniaturization.

Another crucial development in optical domain is the realization of metamaterials, also alternatively known as metastructures. Metamaterials concept was a theoretical framework that followed the postulate on negative-index-materials by Veselago [6]. The intellectual background for the metamaterials concept is based on the manipulation of the electromagnetic field to mimic a material with desired functionality. This was previously achieved mainly via photonic crystals, which are useful for imposing topological constraints on the optical response of the materials. Following Sir John Pendry's work on perfect lensing and cloaking [7, 8], metamaterials have gained widespread attention. However, due to their three-dimensional nature, metamaterials were challenging to fabricate.

The final breakthrough was the creation of the metasurface framework. Rather than imposing phase differential due to propagation in bulk metamaterials, metasurfaces utilized small-scale local "phase injections" at the surface level. Traditionally, metasurfaces are defined as subwavelength-thick versions of metamaterials, analogous in operation (with some differences) but much more compact and scalable - although the limitation on thickness is not strict. Having subwavelength features, they can be used for mimicking a desired functional material in the far-field region. However, metasurfaces can also be used for creating field confinement in a near-field regime. Last ten years of scientific progress took the metasurfaces from niche constructs [9, 10, 11, 12] to competent functional devices [13, 14, 15, 16, 17, 18]. The “metasurface” concept now resonates with generalized use of widely different mechanisms, with the common feature of manipulation of light in a subwavelength scale [19, 20, 21] - resulting in the birth of the meta-optics field. Initial metasurface applications can be viewed as an extension of the phased array concept in millimeter-wave field [22] to higher frequency bands. To construct phase surfaces, Pancharatnam-Berry phase was widely used initially [23, 24]. This was a scheme with applicable to broadband design, but with fundamentally polarization-sensitive operation. Another approach was resonance tuning, including plasmonic structures due to their strong field-enhancing capabilities. Initial designs with plasmonic rods were able to provide only one dipolar resonance, which allows for π phase shift at most; as a result, these designs needed to be operated strictly in reflection mode for full phase control. The phase reach was later extended to 2π with the help of V-antennas capable of supporting two orthogonal modes, sufficient to attain full phase control in transmission mode over the resonance [25, 26]. However, these approaches suffered from an efficiency viewpoint, especially towards visible region, due to the inherent Ohmic losses. Ultimately, the transmission losses were suppressed with the use of dielectric structures supporting Mie resonances instead of plasmonic elements [27, 28]. The use of dielectric elements has also brought about other phase acquisition mechanisms for transmissive optics to the foreground. Additionally, the phase accumulation via guiding was made possible, enabling arbitrarily large phase differentials subject to the aspect ratio limitations in the fabrication processes [13, 29].

Metasurfaces, being diffractive elements, produce their output as an interference pattern of numerous surface waves exiting numerous meta-atoms, a set of discrete unit cells that are repeated to create a desired phase profile at discrete points across the surface. As the meta-atom efficiencies increased with the use of lossless materials, a fundamental problem became more prominent: the coupling of optical wave to the desired diffractive order. This problem has its roots in the generation of the library of distinct meta-atoms. To prevent unwanted scattering coming from the necessarily inhomogeneous placement of different meta-atoms, the meta-atom designs are subject to periodicity and cell-to-cell uncoupling constraints as a convention. Most of the time, these constraints pose a trade-off between interactivity (closely related to functional efficiency) and the purity of steered beam. Highly pure and highly efficient beam-steering was achieved with resonance-tuning approaches, but at the cost of their spectral band of operation [16], which is too narrow. Broadband and efficient metasurfaces operating in the visible region have been thus far lacking.

In this thesis work, to achieve achromatic and highly efficient transmissive optical devices, we present an alternative phase accumulation mechanism that does not require uncoupled operation, enabling continuous sampling of required phase profile and increased functional efficiency. Using identical nanopillars with waveguiding capabilities, here we show how to generate such phase surfaces by tuning the near-field coupling between neighboring elements. Here we also utilized optimization methods to construct the irregular lattices that incorporate the required functionality. As proof-of-concept demonstrations, we designed different metasurfaces operating in the visible region with various functionalities and compared their performance with previous works in the literature.

The thesis contains 4 chapters. In Chapter 2, we provide some background information on metasurfaces, presenting different phase accumulation mechanisms and comparing them in terms of their capabilities and application areas with relevant works in the literature. Afterwards, we present a toy-model phase accumulation mechanism, and justify our model with analytical tools such as homogenization theory and coupled-mode theory.

In Chapter 3, we computationally explore the capabilities of our phase generation mechanism in MODE Waveguide Simulator and FDTD Nanophotonic Simulator. The physics of our proposed cell-less metasurface construction methodology is also explained here. Later, we present methodologies for the generation of achromatic phase differential generation schemes. Based on thee presented schemes, we propose proof-of-concept designs for achromatic focusing in visible region. Two achromatic metalens designs, one cylindrical and one circular, are constructed from the generated library of phase elements. An algorithmic tiling method utilizing optimization methods, used for construction of the required irregular lattices of nanopillars, is then presented. The validations of the individual designs are performed via full electromagnetic computations in ANSYS Lumerical FDTD Nanophotonics Simulator. Finally, the simulation results are presented, and compared with the previous works in the literature.

In Chapter 4, the conclusion of this thesis is presented and the potential realization schemes, along with the future reach of the presented meta-atomless-metasurface concept are provided.

Chapter 2

Overview of phase accumulation mechanisms for metasurfaces

Starting from the examples in phased arrays to the sophisticated multi-functional optical metasurfaces of today, the key role of phase differential across the device plane is fundamental. This is motivated by Huygens' principle: any point on a surface acts as a secondary source dependent on the incident local electromagnetic field, and contribute to collectively producing the next wavefront as the interference pattern of emissions from all the points on the surface. In phased arrays, the local sources are directly controlled by the ability to impose arbitrary phase on the current fed to the antenna. This is not the case for most of frequency-selective-surfaces in general, as the ability to directly control the primary source is not always possible. However, for source-free or passive operation, the electromagnetic response of the local constituents forms the secondary source. Initial examples for generating the aforementioned proxy sources are metal patches of various forms such as split-ring resonators on dielectric substrates.

2.1 Resonance tuning

The imparted phase range heavily depends on the geometrical qualities of the construct, as the secondary sources are actually generated from the multipole moment response of the structures. This is the so-called resonance-tuning approach. At the resonance, which is usually the designed regime of operation, the electromagnetic energy is confined to and interacts strongly with the metastructure. The higher the quality factor of the resonator, the higher interactivity becomes and the narrower the interaction in terms of operation regime and geometry manifests. Consequently, resonance-tuning approaches produce the extremes in efficiency, directionality, or sensitivity in narrow bands. Designs with plasmonic discs and V-antennas, as well as gap resonators such as metal-insulator-metal structures as meta-atom library elements can be found in the literature. For dielectric designs, spheres and cylinders, initially as a monomer but lately in dimer and oligomer formations are used for the creation and tuning of various resonances.

2.2 Pancharatnam-Berry phase

Polarization is a fundamental property of the light. Processes such as free-space propagation or reflection from a boundary have system-dependent eigenstates. For propagation in an isotropic optical crystal, the polarization states are isotropic and as a result, any polarization state is preserved throughout the propagation. Propagation in a birefringent crystal is a system where the anisotropic nature of the crystal shows itself in the polarization eigenstates. The polarization of the system is preserved only if the initial polarization is parallel to the fast or slow axis of the crystal - which are the eigenstates. For the other polarizations, different polarization states experience phase difference as the wave propagates, which results in birefringence.

Pancharatnam-Berry (PB) phase, also known as geometric phase, is the phenomenon where a system going through a cyclic adiabatic process experiences a phase shift dependent on the state change of its Hamiltonian. Pancharatnam explored the phenomenon in 1956 on optical crystals and linked the phase difference to the solid angle covered by the path taken by the light on the Poincare sphere. The geometrical phase was later generalized to quantum systems by Berry. It was also shown that the state change need not to be slow - state changes as light passes through a thin membrane obey the same equations.

The state changes can be represented by Jones calculus:

$$\mathcal{T}(\perp, \|, \theta) = \frac{1}{2}\left(t_{\perp} + t_{\|}\right)\begin{bmatrix}1 & 0\\0 & 1\end{bmatrix} + \frac{1}{2}\left(t_{\perp} - t_{\|}\right)\begin{bmatrix}0 & \exp\left(i2\theta\right)\\ \exp\left(-i2\theta\right) & 0\end{bmatrix} \tag{2.1}$$

where $\mathcal{T}$ expresses the transmitted wave, $t_{\perp,\|}$ denote the eigenstates of the system, and θ is the angular orientation of the system with respect to a fixed reference. $t_{\perp,\|}$ depend on the system in question, and include the polarization- and frequency-dependent coupling coefficients to the eigenstates. PB phase is expressed as the matrix in the second term.

From (2.1), we can notice some characteristics of PB phase. First, if the coupling coefficients and eigenstates are independent of frequency, then PB phase gives an achromatic phase term to the component with cross-coupling. The first term can be minimized by including a half-wave plate to the system. As a result, the phase term can appear purely in the transmitted state. Second, we see that the interactivity of the general system is at most 25%, if only one polarity of the phase is concerned. To see this, note that half of the incident wave goes through the system unperturbed, whereas half of it is coupled to cross-polarized term and acummulates the PB phase. Third, it is easy to see that the exit state is dependent on the incident polarization. If the system is fed by different eigenstates, they will experience phases with opposite signs, i.e., one of them having a phase advance and the other having a phase delay. As the contribution of distinct polarization eigenstates depend on the projection of the incoming polarization state to the system eigenstates, the response will be polarization-dependent.

2.3 Waveguiding phase

Light obeys Fermat's principle as it travels with respect to minimizing the total optical path. Beam shaping and steering are achieved in bulk optical components with the precise shaping of height profile or propagation distance. As the optical path depends on both the propagation distance and the refractive index of the medium, it is also possible to play with the local refractive index to impose a phase differential across the device plane. Initial approaches in this front were simplistic models with local effective indices approximated dependent on the volumetric average of the constituting materials in the meta-atoms. However, these approaches break down if one goes out of the limits of the homogenization theorem, i.e., the scales of the particles approach and exceed the wavelength. Thus, for designs with fill-factor-tuning approaches, the phase differential that is achievable within the regions of approximation of the simple model was limited.

Outside of these bounds, the waveguiding approach is more convenient to use. As the wave propagates in a waveguide, it behaves as if it is propagating in an infinite extent effective medium. Particle-like behavior such as the finiteness in propagation direction, as well as multipole-induced radiation can be lumped together and modelled as radiation modes of the waveguide. For a given guided mode,

$$\Phi(z) = \beta z = n_{eff}\frac{2\pi}{\lambda}z \tag{2.2}$$

where Φ is the phase accumulated due to propagation in the waveguide, β is the λ-dependent propagation constant and z is the propagation distance. A given initial wave, upon being incident to the waveguide, couples to its discrete guided modes and a continuum of radiation modes (leaky modes). The coupling coefficients to individual waveguide modes can be found by taking an overlap integral between the initial wave and the specific mode. The radiation and guiding modes form an orthogonal basis and the coupling coefficients are sufficient to describe the propagation of the energy alongside the waveguide. At the exit planes of the waveguide, the finiteness presents spatial transients that contribute to the radiation modes.

The propagation phase provided by the waveguide is dependent on the solutions to the wave equation in the waveguide. Dependent on the geometry of the waveguide and the spectrum, multiple guiding modes may exist with varying propagation constants. Anisotropy in waveguide cross-section shows itself as mode splitting. Also, a given waveguide mode has dispersion - the guided mode starts as mostly propagating in the low-index medium, and with increasing frequency, is further confined to the regions of higher index. At the frequency extrema, the waveguide dispersion is negligible as it approximates a uniform medium.

In [29], it was shown that meta-structures composed of finite cylinders can be modelled as circular dielectric waveguides. The circular waveguides were operated outside of their resonances, and within the bounds of single-mode operation. By tuning the radii of the individual waveguides, the authors were able to achieve broadband polarization-independent operation between $\lambda = 4.2\,\mu m$ and $4.64.2\,\mu m$. However, the same approach is not sufficient for the visible wavelengths. Below, we explain the reasons with the help of theoretical analysis. [30]

Circular waveguides can be analyzed by solving the boundary conditions for Maxwell's equations. Imagine a circular fiber with an index distribution such as:

$$n(\rho) = \begin{cases} n_{env} = \sqrt{\epsilon_{env}}, & r > a \\ n_{core} = \sqrt{\epsilon_{core}} > n_{env}, & r \leq a \end{cases}$$

where ρ is the radial coordinate, a is the radius of the waveguide core, and $n_{core,env}$ are the refractive indices of core and environment, respectively. All the materials are assumed to be non-magnetic. Cladding is not taken into account and the fiber is modelled as a bare infinite core in the environment. As the profiles are step-index, the general vector wave equations simplify to scalar wave equations for this problem, which are much easier to understand and solve.

As the wave travels in the waveguide, its energy is partially confined in the core, the rest of the wave travels in the environment. Since the wave cannot travel with two different group velocities in the two dielectric media it is confined to, it attains an intermediate group velocity. This condition sets a boundary to the propagation constant β as $\frac{2\pi}{\lambda} n_{env} \leq \beta \leq \frac{2\pi}{\lambda} n_{core}$. Also, the boundary between two mediums should obey Maxwell's equations, thus the tangential fields along the boundary should approach to the same values as one approaches from the core or the environment. For a medium of constant cross-section, the solutions to the wave equations should have variations in the transverse direction, but only a phase factor in the longitudinal direction due to propagation. It is well-known that all the components of electric and magnetic fields for propagating plane waves can be expressed in terms of their E- and H-field components along $\hat{z}$. In cylindrical coordinates of (r, ϕ, z), these relations read

$$E_r = -\frac{i}{\kappa^2}\left(\beta \frac{\partial E_z}{\partial r} + \omega\mu \frac{1}{r}\frac{\partial H_z}{\partial \phi}\right) \tag{2.3}$$

$$E_\phi = -\frac{i}{\kappa^2}\left(\beta \frac{1}{r}\frac{\partial E_z}{\partial \phi} - \omega\mu \frac{\partial H_z}{\partial r}\right) \tag{2.4}$$

$$H_r = -\frac{i}{\kappa^2}\left(\beta \frac{\partial H_z}{\partial r} - \omega\epsilon \frac{1}{r}\frac{\partial E_z}{\partial \phi}\right) \tag{2.5}$$

$$H_\phi = -\frac{i}{\kappa^2}\left(\beta \frac{1}{r}\frac{\partial H_z}{\partial \phi} + \omega\epsilon \frac{\partial H_z}{\partial r}\right) \tag{2.6}$$

where $\kappa^2 = k^2 - \beta^2$ and $k = \omega\sqrt{\epsilon\mu} = k_0 n$. For ray optics purposes, β, κ and k form a Pythagorean triple defining the angle of the wave with respect to $\hat{z}$. The wave equation in the cylindrical coordinates, when expressed in terms of the longitudinal field components, also read

$$\frac{\partial^2 E_z}{\partial r^2} + \frac{1}{r}\frac{\partial E_z}{\partial r} + \frac{1}{r^2}\frac{\partial^2 E_z}{\partial \phi^2} + \kappa^2 E_z = 0 \tag{2.7}$$

$$\frac{\partial^2 H_z}{\partial r^2} + \frac{1}{r}\frac{\partial H_z}{\partial r} + \frac{1}{r^2}\frac{\partial^2 H_z}{\partial \phi^2} + \kappa^2 H_z = 0 \tag{2.8}$$

Assuming functional form of $\Psi = \mathcal{R}(r)\exp^{i\nu\phi}\exp^{i(\omega t - \beta z)}$ for the longitudinal fields, we obtain the differential equation

$$\frac{d^2\mathcal{R}}{dr^2} + \frac{1}{r}\frac{d\mathcal{R}}{dr} + \left(\kappa^2 - \frac{\nu^2}{r^2}\right)\mathcal{R} = 0 \tag{2.9}$$

The solutions to this differential equation is Bessel functions with integer order ν to satisfy periodicity of 2π. Two independent solutions exist, with a plethora of different conventions across the optical waveguide community. We are going to follow Marcuse's notation [31] and use Bessel function of the first kind $J_\nu(\kappa r)$

for $r \to 0$ and Hankel function of the first kind $H_\nu^{(1)}(\kappa r)$ for $r \to \infty$. J_ν always remains finite, whereas $H_\nu^{(1)}$ diverges as $r = 0$ and approximates a travelling wave propagating towards $-\hat{r}$ as r increases - an incoming wave from infinity. For imaginary arguments, $H_\nu^{(1)}(i\gamma r)$ approximates exponential decay with $\exp^{-\gamma r}$ in the large argument limit. With these longitudinal solutions the complete field components can be constructed from J_ν in the core and $H_\nu^{(1)}$ in the environment. For $r < a$,

$$E_z = AJ_\nu(\kappa r)\exp^{i\nu\phi} \tag{2.10}$$

$$H_z = BJ_\nu(\kappa r)\exp^{i\nu\phi} \tag{2.11}$$

$$E_r = -\frac{i}{\kappa^2}\left[\beta\kappa AJ_\nu'(\kappa r) + i\omega\mu_0\frac{\nu}{r}BJ_\nu(\kappa r)\right]\exp^{i\nu\phi} \tag{2.12}$$

$$E_\phi = -\frac{i}{\kappa^2}\left[i\beta\frac{\nu}{r}AJ_\nu(\kappa r) - \kappa\omega\mu_0 BJ_\nu'(\kappa r)\right]\exp^{i\nu\phi} \tag{2.13}$$

$$H_r = -\frac{i}{\kappa^2}\left[-i\omega\epsilon_{core}\frac{\nu}{r}AJ_\nu(\kappa r) + \kappa\beta BJ_\nu'(\kappa r)\right]\exp^{i\nu\phi} \tag{2.14}$$

$$H_\phi = -\frac{i}{\kappa^2}\left[\kappa\omega\epsilon_{core}AJ_\nu'(\kappa r) + i\beta\frac{\nu}{r}BJ_\nu(\kappa r)\right]\exp^{i\nu\phi} \tag{2.15}$$

and for $r > a$

$$E_z = CH_\nu^{(1)}(i\gamma r)\exp^{i\nu\phi} \tag{2.16}$$

$$H_z = DH_\nu^{(1)}(i\gamma r)\exp^{i\nu\phi} \tag{2.17}$$

$$E_r = -\frac{1}{\gamma^2}\left[\beta\gamma CH_\nu^{(1)'}(i\gamma r) + \omega\mu_0\frac{\nu}{r}DH_\nu^{(1)}(i\gamma r)\right]\exp^{i\nu\phi} \tag{2.18}$$

$$E_\phi = -\frac{1}{\gamma^2}\left[\beta\frac{\nu}{r}CH_\nu^{(1)}(i\gamma r) - \gamma\omega\mu_0 DH_\nu^{(1)'}(i\gamma r)\right]\exp^{i\nu\phi} \tag{2.19}$$

$$H_r = -\frac{1}{\gamma^2}\left[-\omega\epsilon_{env}\frac{\nu}{r}CH_\nu^{(1)}(i\gamma r) + \gamma\beta DH_\nu^{(1)'}(i\gamma r)\right]\exp^{i\nu\phi} \tag{2.20}$$

$$H_\phi = -\frac{1}{\gamma^2}\left[\gamma\omega\epsilon_{env}CH_\nu^{(1)'}(i\gamma r) + \beta\frac{\nu}{r}DH_\nu^{(1)}(i\gamma r)\right]\exp^{i\nu\phi} \tag{2.21}$$

with the decay constant $\gamma^2 = \beta^2 - n_{env}^2 k_0^2$. The solutions to the wave equations also need to satisfy the boundary conditions. Since the system is source-free, the boundary conditions correspond to the equivalence of tangential fields at the surface $r = a$, i.e., E_z, H_z, E_ϕ, H_ϕ should be continuous at the boundary. By equating the corresponding field components across the boundary, we reach the solutions via

$$\left(\frac{n_{core}^2}{n_{env}^2}\frac{a\gamma^2}{\kappa}\frac{J_\nu'(\kappa a)}{J_\nu(\kappa a)}+i\gamma a\frac{H_\nu^{(1)'}(i\gamma a)}{H_\nu^{(1)}(i\gamma a)}\right)\left(\frac{a\gamma^2}{\kappa}\frac{J_\nu'(\kappa a)}{J_\nu(\kappa a)}+i\gamma a\frac{H_\nu^{(1)'}(i\gamma a)}{H_\nu^{(1)}(i\gamma a)}\right)= \left[\nu\left(\frac{n_{core}^2}{n_{env}^2}-1\right)\frac{\beta k_0 n_{env}}{\kappa^2}\right]^2 \tag{2.22}$$

with

$$\frac{C}{A}=\frac{D}{B}=\frac{J_\nu(\kappa a)}{H_\nu^{(1)}(i\gamma a)} \tag{2.23}$$

where A and B denote the field amplitudes for longitudinal E- and H- fields, respectively. For arbitrary ν, it is not possible to find solutions that make A or B zero. However, for the specific case of $\nu = 0$, the right-hand side of the eigenvalue equation vanishes and two sets of solutions appear after simplification with the usage of Bessel function family identities ($J_0' = -J_1$, $H_0^{(1)'} = -H_1^{(1)}$)

$$\left(\frac{n_{core}^2}{n_{env}^2}\frac{\gamma}{\kappa}\frac{J_\nu'(\kappa a)}{J_\nu(\kappa a)}+i\frac{H_\nu^{(1)'}(i\gamma a)}{H_\nu^{(1)}(i\gamma a)}\right)=0 \qquad \text{(TM case)} \tag{2.24}$$

$$\left(\frac{\gamma}{\kappa}\frac{J_\nu'(\kappa a)}{J_\nu(\kappa a)}+i\frac{H_\nu^{(1)'}(i\gamma a)}{H_\nu^{(1)}(i\gamma a)}\right)=0 \qquad \text{(TE case)} \tag{2.25}$$

For other ν, the guided modes exhibit hybrid nature, and are denoted with HE or EH modes depending on the dominant contributing longitudinal field. From the viewpoint of ray optics, TE and TM modes correspond to the rays that are normally incident on the waveguide boundary (implying the rays pass through the waveguide center, i.e., meridional rays) and the hybrid modes correspond to rays that are oblique to the boundary and change orientation as they propagate in the waveguide (skew rays) - which is apparent in their ϕ-dependency.

All the modes outside of the fundamental HE_{11} mode has cutoffs. A useful constant for the approximate determination for the availability of the modes is the fiber parameter $V = \frac{2\pi}{\lambda}a\sqrt{n_{core}^2 - n_{env}^2}$. HE_{11} mode does not have a cutoff, while TE and TM modes have cutoffs at $V = 2.405$. All successive higher-order modes have cutoffs depending on the mth zero of the Bessel function.

2.3.1 Dispersion

As V increases, the waveguide can support more oblique rays inside. This also implies it confines the already-guided modes better in the core. For a fiber of a constant geometry, V increases with the wavevector, i.e., shorter wavelengths get to be confined, and their resulting propagation constants are closer to that of the core. This shows itself in the dispersion relation of the mode: the effective index of the given mode starts from n_{env} from the cutoff condition ($\kappa a = 0, \gamma a = V$) and progressively increases to n_{core} as the frequency increases. On a $\omega - \beta$ plot, the solutions start by following the light line from the low-index medium side, and then approach the light line for high-index medium. The shape of waveguide dispersion curve is akin to the normal dispersion curves $\left(\frac{\partial n}{\partial \lambda} < 0\right)$.

On top of the waveguide dispersion, the fiber material (and cladding, if present) have dispersive properties due to their material properties. As the guided power is not completely confined to the core, the effective material dispersion is a weighted average of the dispersions of the core and cladding. For lossless dielectric materials outside of their material resonances, the dispersion relation can be expressed with Cauchy model:

$$n(\lambda) = A + \frac{B}{\lambda^2} + \frac{C}{\lambda^4} \dots \tag{2.26}$$

Cauchy model is empirical, but commonly used for scientific practices. For $A, B, C > 0$, it leads to normal dispersion $\left(\frac{\partial n}{\partial \lambda} < 0\right)$. Material dispersion and waveguide dispersion collectively is called intramodel dispersion (as it describes the dispersion of a single guided mode), whereas the differences between different guided modes constitute intermodal dispersion (not applicable to single-mode waveguides).

2.3.2 Dispersion compensation

For our intents and purposes, bare circular single-mode waveguides composed of lossless dielectrics present normal dispersion from both waveguiding and waveguide material itself. Achromatic waveguiding, which will result in achromatic phase differential generation, requires compensation of the normal dispersion with some mechanism with anomalous dispersion generation. In the previous years, it was shown that dispersion compensation over wide bandwidths can be achieved via coupling [32, 33]. Coupling to adjacent waveguides present a channel to the power flow, with the coupling coefficient between the waveguides acting as additional propagation constants. Additionally, the guided mode is more confined to the gap between the waveguides [34]. The wavefunctions in the gap region acquire non-decaying contributions as a result of the change in boundary conditions: as the gap region is finite, exponentially increasing solutions also contribute to the wavefunctions.

Let a be the radius of the circular waveguide we would like to couple to the neighbors, between the wavelength region of $\lambda_{min} - \lambda_{max}$. Let n_{core} be a monotonically decreasing function of the wavelength in this regime and $n_{env} < n_{core}$ be the dispersionless refractive index of the gap. We have

$$V(\lambda) = 2\pi n_{env} \frac{a}{\lambda} \sqrt{\frac{n_{core}^2(\lambda)}{n_{env}^2} - 1} \tag{2.27}$$

We choose a such that $V(\lambda)$ does not exceed the single-mode boundary of 2.405.

The confinement factor η for a given mode, defined as

$$\eta_{\nu m} = \frac{\int_{A_{core}} \mathbf{E}_{\nu \mathbf{m}} \times \mathbf{H}^*_{\nu \mathbf{m}} \cdot \hat{\mathbf{z}}\, dA}{\int_{A_\infty} \mathbf{E}_{\nu \mathbf{m}} \times \mathbf{H}^*_{\nu \mathbf{m}} \cdot \hat{\mathbf{z}}\, dA} \tag{2.28}$$

is a monotonically increasing function of V for constant refractive indices. This is not the situation for our case, but for our simple model, we will assume the dependence of η on V is satisfied. In (2.28), A_{core} is the core region; $E_{\nu m}, H_{\nu m}$ are the electric and magnetic field vectors of the guided mode with order ν and index m. The relations between n_{eff} and η is shown to be nonlinear for single-mode fibers [35], and the dependence is shown to be linear with the ratio of the integrated fields, rather than the integrated power. This is reminiscent of homogenization theories with field-averaged effective index values.

Now let another waveguide be present next to the initial waveguide. For ease of analysis, assume the waveguides to be identical. As the gap between the waveguides become smaller, the evanescent fields in the gap region become coupled. The effect will be symmetrical as the waveguides are symmetric, i.e., the power will not oscillate between two channels, but rather move synchronously. Analogous to slot waveguide examples in the literature [34], where the exponentially decaying fields in the gap region collectively add up to solutions with cosh dependence, circular waveguides with $H_\nu^{(1)}$ solutions in the gap collectively add up to non-vanishing fields in the gap.

The dependence of effective index of an isolated waveguide on wavelength is expressed as

$$n_{eff}(\lambda) = \frac{n_{env}F_{env} + n_{core}F_{core}}{F_{core} + F_{env}} \tag{2.29}$$

$$F_{core} = \int_0^a J_0(\kappa r) r \, dr \tag{2.30}$$

$$F_{env} = \frac{J_0(\kappa a)}{H_0^{(1)}(i\gamma a)} \int_a^\infty H_0^{(1)}(i\gamma r) r \, dr \tag{2.31}$$

where $F_{core,env}$ is the field integral in the core and environment, respectively. The cylindrical symmetry is used for removing the angular dependence on ϕ and negating the common coefficients from the field integrals. The coefficient before the field integral in the environment comes from the ratio of the amplitudes of the solutions, i.e., C/A.

As the independent effects on dispersion from guiding index, material refractive index and coupling change continuously with the wavelength, we can model their contributions to the dispersion with their independent effects and residual higher-order correction G:

$$\begin{aligned} D(\lambda, d_{neigh}, n_{core}) =& D_{uncoupled}(\lambda, n_{core}) + D_{coupling}(\lambda, n_{core}, d_{neigh}) \\ & + G(\lambda, d_{neigh}, n_{core}) \end{aligned} \tag{2.32}$$

$$D_{uncoupled}(\lambda, n_{core}) = \frac{\partial n_{eff}(\lambda)}{\partial \lambda} \tag{2.33}$$

where $D_{coupling}$ is the dispersion due to coupling. The effect of coupling on the effective index a monotonically decreasing function of the confinement factor or field integral ratio $\frac{F_{core}}{F_{core} + F_{env}}$, because the power funnelled to the coupling channels decrease with confinement. To see this, we note γ is a decreasing function of the wavelength . As in normalized form, γa approximates the rate of decay for the evanescent wave ate one wavelength of propagation, as $H_{\nu}^{(1)}(i\gamma a)$ has a form akin to exponential decay. Thus, for longer λ, the field decays more slowly in the gap, which results in larger coupling. We model this by stating $\frac{\partial n_{coupling}}{\partial \lambda} > 0$, or equivalently $D_{coupling} > 0$. On the other side, the dispersion of the uncoupled fiber becomes less negative with the field integral ratio (thus with decreasing λ), as the effective index is the field-weighted average of n_{core} and dispersionless n_{env}. The higher-order correction terms are not analyzed, as the interdependence is not significant for the purpose of this thesis. Finally, we notice the first-order terms of (2.32) have opposite signs, and hypothesize that it is possible to arrange a, λ, n_{core} and d_{neigh} so that zero dispersion can be achieved with small enough higher-order correction terms, as we shall use later in the thesis.

2.3.3 Coupled mode theory analysis

The effect of proximity for two identical waveguides can also be analyzed with the help of coupled mode theory. We will follow the formalism in [31] for the general derivation for the coupled mode equations, and then present our geometry as a specifically symmetric case.

Assume that two waveguides have waveguide solutions of $\mathbf{E_1}, \mathbf{H_1}$ and $\mathbf{E_2}, \mathbf{H_2}$ in the absence of each other. For identical waveguides, which is the basis of our structures, the uncoupled solutions are of the same form with a coordinate translation, but for a general case, the solutions are different with different field profiles and propagation constants. We can express the total field as

$$\mathbf{E} = A_1(z)\mathbf{E_1} + A_2(z)\mathbf{E_2} \tag{2.34}$$

$$\mathbf{H} = A_1(z)\mathbf{H_1} + A_2(z)\mathbf{H_2} \tag{2.35}$$

accurate to the first order.

The refractive index profile $n(r)$ is

$$n^2 = (n^2_{core_1}(r) - n^2_{env}) + (n^2_{core_2}(r) - n^2_{env}) + n^2_{env} \tag{2.36}$$

We will impose the limiting condition of non-dissipativeness: the total power should be conserved, i.e., $\dfrac{\partial |A_1(z)|^2 + |A_2(z)|^2}{\partial z} = 0$.

The fields satisfy Maxwell's equations. Thus,

$$\nabla \times \mathbf{H} = i\omega\epsilon_0 n^2 \mathbf{E} \tag{2.37}$$

$$\nabla \times \mathbf{E} = -i\omega\mu_0 n^2 \mathbf{H} \tag{2.38}$$

Substituting (2.34) into (2.37),

$$A_1 \left[\nabla_t \times \mathbf{H_1} - i\beta_1(\mathbf{z} \times \mathbf{H_1})\right] + \frac{\partial A_1}{\partial z}(\mathbf{z} \times \mathbf{H_1}) - i\omega\epsilon_0 n^2 A_1 \mathbf{E_1} \tag{2.39}$$

$$+A_2 \left[\nabla_t \times \mathbf{H_2} - i\beta_2(\mathbf{z} \times \mathbf{H_2})\right] + \frac{\partial A_2}{\partial z}(\mathbf{z} \times \mathbf{H_2}) - i\omega\epsilon_0 n^2 A_2 \mathbf{E_2} = 0$$

$$A_1 \left[\nabla_t \times \mathbf{E_1} - i\beta_1(\mathbf{z} \times \mathbf{E_1})\right] + \frac{\partial A_1}{\partial z}(\mathbf{z} \times \mathbf{E_1}) + i\omega\mu_0 n^2 A_1 \mathbf{H_1} \tag{2.40}$$

$$+A_2 \left[\nabla_t \times \mathbf{E_2} - i\beta_2(\mathbf{z} \times \mathbf{E_2})\right] + \frac{\partial A_2}{\partial z}(\mathbf{z} \times \mathbf{E_2}) + i\omega\mu_0 n^2 A_2 \mathbf{H_2} = 0$$

These equations can be simplified as E_1, H_1 and E_2, H_2 independently satisfy the wave equations for n_{core_1} and n_{core_2}, respectively.

$$\frac{\partial A_1}{\partial z}(\mathbf{z} \times \mathbf{H_1}) - i\omega\epsilon_0 \left(n^2_{core_2} - n^2_{env}\right) A_1 \mathbf{E_1} \tag{2.41}$$

$$+\frac{\partial A_2}{\partial z}(\mathbf{z} \times \mathbf{H_1}) - i\omega\epsilon_0 (n^2_{core_1} - n^2_{env}) A_2 \mathbf{E_2} = 0$$

$$\frac{\partial A_1}{\partial z}(\mathbf{z} \times \mathbf{E_1}) + \frac{\partial A_2}{\partial z}(\mathbf{z} \times \mathbf{E_2}) = 0 \tag{2.42}$$

After subtracting the scalar products $\{\mathbf{E_1^*}, (2.42)\}$ and $\{\mathbf{H_1^*}, (2.43)\}$ and keeping the terms of first order,

$$\frac{\partial A_1}{\partial z} = ic_1 A_2 \exp^{i(\beta_1-\beta_2)z} \tag{2.43}$$
$$\frac{\partial A_2}{\partial z} = ic_2 A_1 \exp^{i(\beta_2-\beta_1)z} \tag{2.44}$$

where

$$c_1 = -\omega\epsilon_0 \frac{\int_{A_\infty}(n_{core_1}^2 - n_{env}^2)\mathbf{e_1^*}\cdot\mathbf{e_2}\,dA}{\int_{A_\infty}(\mathbf{e_1^*}\times\mathbf{h_1}+\mathbf{e_1}\times\mathbf{h_1^*})\cdot\mathbf{z}\,dA} \tag{2.45}$$
$$c_2 = -\omega\epsilon_0 \frac{\int_{A_\infty}(n_{core_2}^2 - n_{env}^2)\mathbf{e_2^*}\cdot\mathbf{e_1}\,dA}{\int_{A_\infty}(\mathbf{e_2^*}\times\mathbf{h_2}+\mathbf{e_2}\times\mathbf{h_2^*})\cdot\mathbf{z}\,dA} \tag{2.46}$$

with e, h denoting the fields without their z-dependence. Alternatively, the relationships can be written with the explicit phase factor, which results in $\partial a_{1,2}/\partial z = -i\beta_{1,2}a_{1,2} + ic_{1,2}a_{2,1}$. This alternative form is useful because it shows the validity of coupling as an additional phase element.

Considering our special case, where the waveguides are identical ($\beta_1 = \beta_2$) with purely real core and environment refractive indices, the denominator is equal to $4P_{guided}$ and the modal fields are equal within a coordinate transformation. Thus, the coupling coefficients are equal and real (energy conservation). Since the coupling coefficients are purely real, there is no energy transfer between two modes, but rather a phase accumulation. Looking at the alternative form, it is clear that the additional propagation constant $\Delta\beta$ is equal to c. For the relatively simple geometry of slab waveguides with thicknesses of $2a$ and edge-to-edge separation d_{e2e}, the additional propagation constant has the form of

$$\Delta\beta = \frac{\kappa^2\gamma^2}{\kappa^2+\gamma^2}\frac{1}{\beta(1+\gamma a)}\exp^{-\gamma d_{e2e}} \tag{2.47}$$

For small a, the term in the denominator can be thought of as the first-order Taylor expansion of $\exp^{\gamma a}$, resulting in $\exp^{-\gamma(a+d_{e2e})}$, an exponential increase with decreasing nearest-neighbor distance. For weakly guided modes, $\kappa >> \gamma$, simplifying as $\Delta\beta \approx (\gamma^2/\beta)\exp^{-\gamma(d_{e2e}+a)}$. Compared to the multiplicative dependency on γ and β, the exponential factor with small γ and d_{e2e} dominates at the long wavelength limit, which corresponds to relatively large propagation constant differentials. This analysis forms the backbone of our claim that coupling can be utilized as an anomalous dispersion contributor.

However, the evaluation of (2.46) for circular waveguides that placed in 2D lattices is challenging from multiple perspectives. First, the individual modal fields for different waveguides should be written in the same coordinate frame, with the cylindrical Bessel and Hankel functions expanded with the help of addition theorems. Tedious it may be, the expansions can be written analytically, but solving the integrals still requires the limitation $d_{e2e} >> a$. It seems more practical to attack the problem from a computational point of view, rather than trying to find analytical solutions. This decision is motivated based on the practical problem in fabrication of metasurfaces: Dispersionless waveguiding should be accompanied with a phase differential generation scheme capable of generating large n_{eff} differences, as the aspect ratios of the structures are limited by fabrication equipment limitations, as well as the mechanical durability of the devised nanostructures. It is indeed probable that the approximation conditions for analytical solutions may not hold for geometries capable of generating large propagation constant differentials via strong near-field coupling. In the following chapter, we will numerically explore the achievable phase differentials via waveguide computations.

Chapter 3

Achromatic near-field-coupled metasurfaces constituted of tiling of identical dielectric waveguides

This chapter is based on our publication "'Meta atom-less' architecture based on an irregular continuous fabric of coupling-tuned identical nanopillars enables highly efficient and achromatic metasurfaces" **H. B. Yağcı** and H. V. Demir, Appl. Phys. Lett. 118, 081105 (2021) [1]. Adapted (or "Reproduced in part") with permission from American Institute of Physics. Copyright 2021 American Institute of Physics.

3.1 Trade-off between efficiency and bandwidth

As explained in Chapter 2, various approaches exist in the literature for generation of phase discontinuities across the metasurface. Common functionalities that were implemented with metasurfaces ranged from holograms to lenses. "Metasurface" became an umbrella term for designs with function-tailored tightly-placed structures of repeating unit cells that acted collectively. Initial approaches were focused on manipulation or detection of signals for systems where the base response of the existing structures was either too weak or the structures were too insensitive. To that end, high-Q resonators proved to be extremely effective tools, as they were able to interact with incoming beam at specific wavelengths strongly and their response was highly sensitive to the surroundings and/or the spectrum. Their chromatic nature, however, was a setback for broadband designs. For broadband designs, the polarization-converting schemes suffer from low interactivity - additionally, the meta-atom designs included uncoupled unit cells to neglect the effect of nearest-neighbor coupling. Uncoupled elements, when placed next to neighboring cells, did not result in notable change of behavior of the neighbors or nearly added cells, which was desirable to keep the design process simple. However, this implied that the unit cells must incorporate relatively large gaps that would "isolate" individual meta-atoms from interacting. As a result, such designs suffer low functional efficiency: the incoming wave is partially exposed to the functionality at the output of the device. This trade-off for broadband designs is more significant in the visible region because of the limitations on available high-index materials and large operation bandwidth. Hence was the problem of efficiency for broadband designs in the visible region.

In Chapter 2, we have proposed a phase acquisition scheme that utilizes near-field coupling of single-mode circular waveguides to rid of the inter-modal dispersion and provide achromatic phase differential generation. We hypothesize that utilization of coupling between the elements enables close packing of phase elements and increases the interactivity while offering a solution to the bandwidth-efficiency trade-off. We propose closely-coupled dielectric nanopillars with continuously-tuned interactivity as a paradigm shift in building a scatterer architecture of metasurfaces, which we coined as meta-atomless metasurfaces (MAMs). We intentionally avoided any internal or external resonances to guarantee achromaticity and relied only on the coupling between our nanopillars operating in guiding mode.

In this chapter, we parametrize our near-field coupled waveguides and show numerical results on the achromatic performance, as well as the total effective index difference across different levels of coupling. We choose TiO_2 as the waveguide material, due to its band-gap residing in UV region and its relatively high refractive index in the visible wavelengths. TiO_2 has relatively minor absorption in 400-700 nm range, making it effectively a lossless dielectric that can be modelled with Cauchy model. As the surrounding medium, we conveniently choose air as it is dispersionless. We limit the radius of the waveguide we use, as multiple propagation modes occurring at any wavelength in the design spectrum would otherwise result in coupling to unwanted modes that cause inter-modal dispersion. Using the refractive index data [2], we find the maximum allowed waveguide radius as

$$a_{max} = \min \left(\frac{V_{cutoff}}{(2\pi/\lambda)\sqrt{n^2_{\mathrm{TiO_2}}(\lambda) - 1}} \right) \approx 60\,\mathrm{nm} \tag{3.1}$$

There is no guarantee that coupling of the waveguides will not result in additional guided modes, as the pre-cutoff leaky modes can turn into guided modes with the help of the periodic boundaries. However, it seems unlikely for our geometry, as the boundaries are circular and the coupling is not circularly symmetric as in a hollow-core fiber.

After selecting the geometry for our waveguides, we also select the geometry of coupling. For 2-D tiling of waveguides with circular cross section, the most common lattice generation schemes involve rectangular and triangular or hexagonal lattice, as well as square lattice as a specific case of rectangular stacking. Parameterizing the nearest-neighbor distances as $\{d_1, d_2\}$ for the former and d_1 in the latter two, we state our problem as finding $d_{1,2}$ such that the absolute dispersion $|D(\mathbf{d})|$ is minimized and the index differential $n_{eff}(\mathbf{d}) - n_{eff}(\mathbf{d}')$ is maximized at the same time.

3.2 Rectangular lattice stacking

3.2.1 Waveguide simulations

To calculate the effective indices, we used ANSYS MODE Waveguide Simulator with the parameters defined in the previous section. The coupling directions for rectangular lattice are taken to be along $\hat{x}$ and $\hat{y}$, Periodic boundary conditions were used for the boundaries in $\hat{x}$ and $\hat{y}$. To explore the effect of polarization, input excitations with orthogonal polarization must be simulated independently; these orthogonal polarization directions were chosen to be parallel to $\hat{x}$ and $\hat{y}$ for convenience. Rectangular mesh with adaptive size was used throughout the waveguide simulations to speed up the simulations for waveguides that are not in the immediate vicinity of each other. The effective index of the structure is provided by the solver following the waveguide calculations. Instead of using approximations to calculate effective indices and dispersion for a given mode as wavelength changes, the field mesh was calculated from scratch to prevent unpredictable errors.

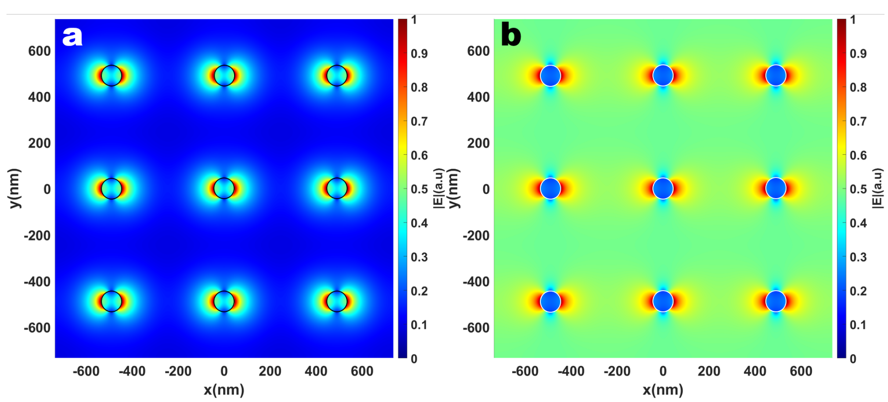

Figure 3.1: Spatial electric field amplitude distribution map across the periodic TiO_2 waveguide cross-section. Waveguide boundaries are marked with overlays with contrasting colors. Here the inter-waveguide distance is 400 nm, the waveguide radius is 45 nm, the input excitation is polarized along $\hat{x}$ and λ are **a** 400 nm **b** 700 nm. Adopted with permission from [1]. Copyright 2021 American Institute of Physics.

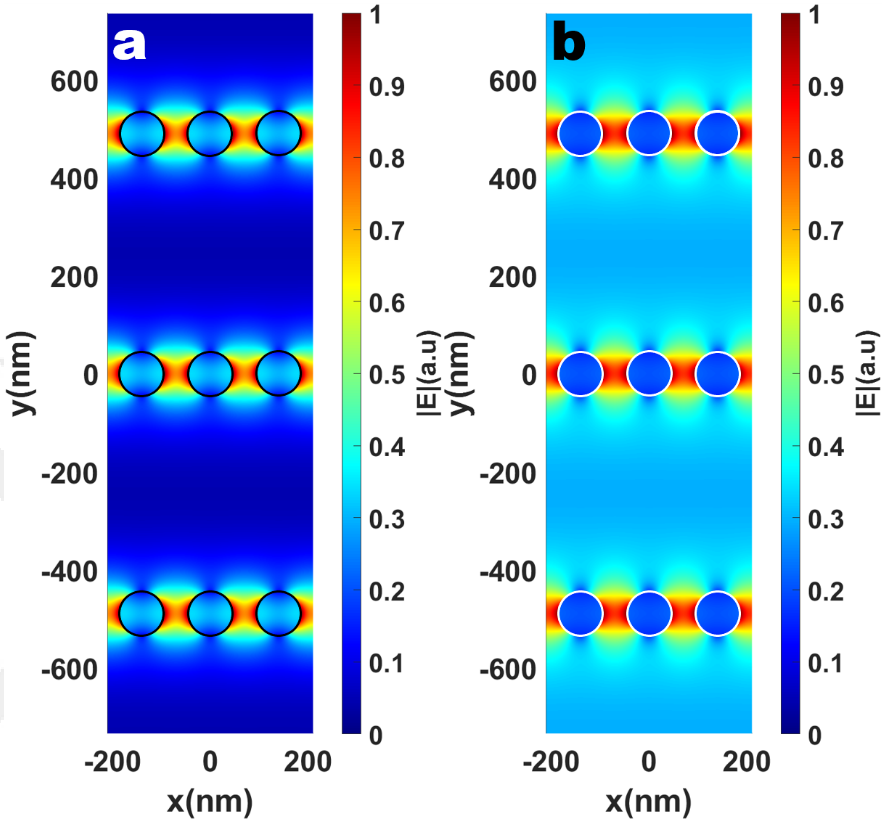

Figure 3.2: Spatial electric field amplitude distribution map across the periodic TiO_2 waveguide cross-section. Waveguide boundaries are marked with overlays with contrasting colors. Here the inter-waveguide distance is 50 nm along the direction parallel to input polarization and 400 nm along the direction perpendicular to input polarization. The waveguide radius is 45 nm, the input excitation is polarized along $\hat{x}$ and λ are **a** 400 nm **b** 700 nm. Adopted with permission from [1]. Copyright 2021 American Institute of Physics.

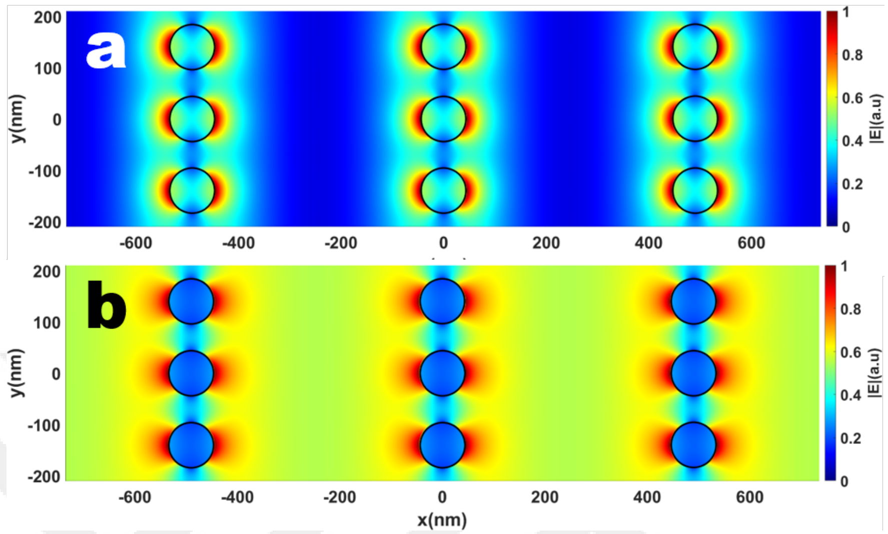

Figure 3.3: Spatial electric field amplitude distribution map across the periodic TiO_2 waveguide cross-section. Waveguide boundaries are marked with overlays with contrasting colors. Here the inter-waveguide distance is 400 nm for parallel direction to input polarization and 50 nm for perpendicular direction. The waveguide radius is 45 nm, the input excitation is polarized along $\hat{x}$ and λ are **a** 400 nm **b** 700 nm. Adopted with permission from [1]. Copyright 2021 American Institute of Physics.

The field distributions for completely uncoupled geometries for wavelength extrema are shown in Figure 3.1. Comparing the left and right panels, it is clear that the wave is more confined for $\lambda = 400$ nm - the field integral ratio F_{core}/F_{env} is larger. On the other side, for wavelength maxima, the fields leak to the gap and couple to neighboring cells even at this distance.

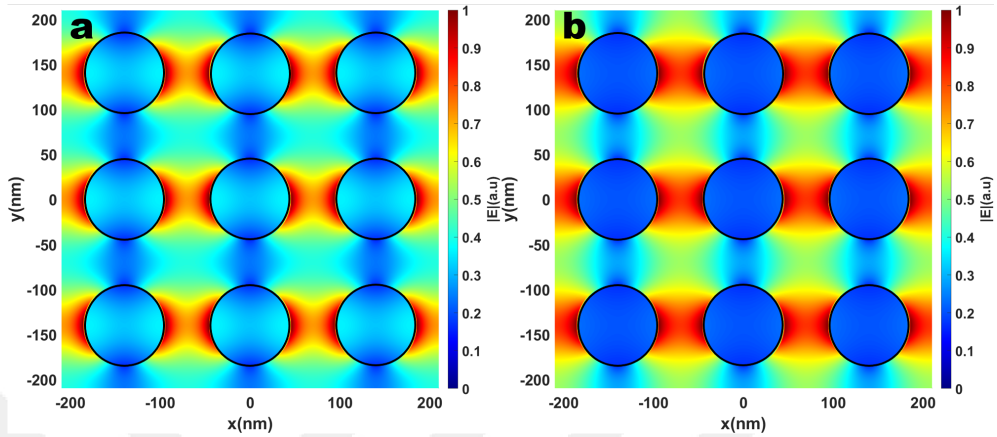

Figure 3.4: Spatial electric field amplitude distribution map across the periodic TiO_2 waveguide cross-section. Here the waveguide boundaries are marked with overlays with contrasting colors. The inter-waveguide distance is 50 nm, the waveguide radius is 45 nm, input excitation is polarized along $\hat{x}$ and λ are **a** 400 nm **b** 700 nm. Adopted with permission from [1]. Copyright 2021 American Institute of Physics.

Coupling results in increased field in the gap region. In Figure 3.2, the case of near-field coupling along the direction parallel to input polarization direction (dubbed as parallel-coupled from now on) is presented for wavelength extrema. After comparing Figures 3.1**a** and 3.2**a**, we can notice the field intensity in the core getting funneled to the gap region due to the coupling. If the waveguides are placed such that they are coupled in the direction perpendicular to the input polarization (dubbed as orthogonal-coupled), the field enhancement in the gap region is more subtle. This case is shown in Figure 3.3. Again, comparison of field distributions shows that the field confinement and hence the field integral ratio is of an intermediate case between uncoupled and parallel-coupled cases. Lastly, the fully coupled case is shown in Figure 3.4. The field enhancement in the inter-waveguide gap is more pronounced for long-wavelength limit, which is our hypothesized mechanism for dispersion compensation.

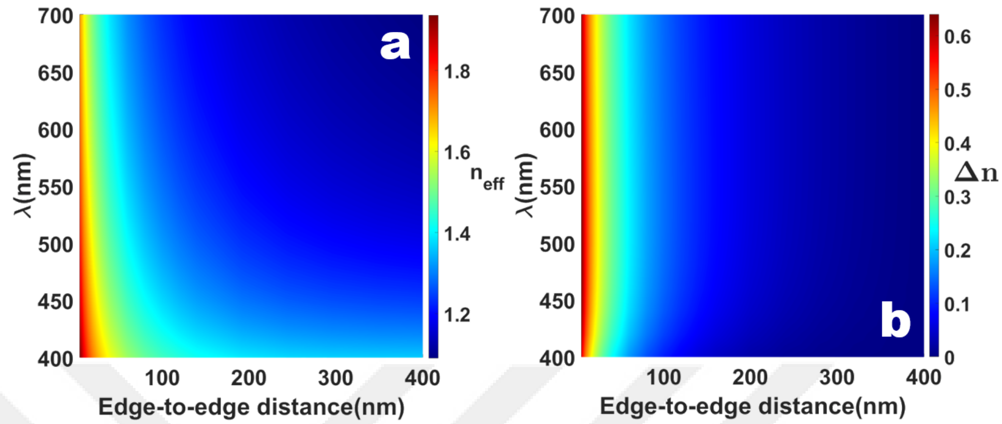

Figure 3.5: **a** Effective refractive index versus varying parallel-coupling distance d_1 and wavelength λ, numerically calculated from simulations made with ANSYS MODE Waveguide Simulator. Orthogonal-coupling distance is set to $d_2 = 30\,\text{nm}$. **b** Effective index difference for the same parameter space, the reference case taken as parallel-uncoupled case ($d_1 = 400\,\text{nm}$). Adopted with permission from [1]. Copyright 2021 American Institute of Physics.

We chose the rectangular stacking as our geometry, as the square lattice generation scheme is complex for squares sub-elements of different sizes, and existing algorithms do not prioritize generation of specifically designed lattices [36]. Based on our explanation in Chapter 2, this allows us to control the contribution of dispersive waveguide material to n_{eff}, whose dispersive effects can be negated with anomalous dispersion caused via the coupling. To this end, $d_2 = 30\,\text{nm}$ was chosen as the optimal orthogonal-coupling distance providing minimal dispersion. To calculate the effective index map for parameter space comprised of parallel-coupling distance d_1 and λ, the waveguide simulations were solved numerically for the whole parameter space. The parallel-coupling distance d_1 varying from 5 to 400 nm was used for tuning the coupling. Figure 3.5 displays n_{eff} and Δn_{eff} maps for varying d_1 and λ. The left panel shows chromatic and coupling-dependent changes in n_{eff}, however, the effective index differential is mostly achromatic, decreasing at the short-wavelength limit.

3.2.2 Confirmation with full electromagnetic solutions

Our approach, however logical it may be, is an approximation. Finite nanocylinders are not infinite waveguides; fibers have spatial transients towards their end faces. Also, the effect of substrate which will host the nanocylinders cannot be explored with waveguide simulations. For this purpose, we also model the nanocylinders in full electromagnetic simulations. We hypothesize that the radiation modes of coupled cylindrical waveguides and scattering from nanocylinders are analogous, and the total phase imparted by the nanocylinders is equivalent to waveguiding phase acquired by the light as it passes through.

The nanocylinder geometry can be seen in Figure 3.6. In our simulations, h was taken as 600 nm for convenience. However, the waveguiding approach is only limited with the achievable aspect ratio, as the object extent in propagation direction increases the phase differential, which is desired. The response of the cells were simulated over the whole 400-700 nm range, with periodic boundary conditions in $\hat{x}, \hat{y}$ boundaries and PML boundary conditions in $\hat{z}$. The substrate was chosen as quartz, and Palik's quartz refractive index data was used from the solver library. A broadband plane wave excitation with propagation direction along $+\hat{z}$ was injected within substrate. With the help of a field monitor placed 50 nm above the top end of the nanocylinder, the response was captured. Fields on the near-field monitor were then projected to far-field ($z = 10\,\mu\text{m}, x = y = 0$) via *farfieldexact3d* function in Lumerical library and propagation phase in the substrate and air were subtracted from the phase of the projected wave. The remaining phase gives the phase response of the nanocylinders and the transmission from the monitor gives the transmittance of the nanocylinder. The results of these full electromagnetic simulations can be seen in Figure 3.7. The phase differential versus λ and d_1 is given in Figure 3.7(a). This result is compared with the waveguiding phase, calculated via $\Phi(d_1, \lambda, \Delta h) = 2\pi n_{eff}(d_1, \lambda)\dfrac{\Delta h}{\lambda}$, where $n_{eff}(d_1, \lambda)$ is taken from Figure 3.5(b). From the similarity of phase profiles, we can conclude that our approximation is valid for these geometries. The transmission results show a small dip in a specific region, whose effect is also visible in panel (a) as the additional phase coverage. This effect is undesired, and this region is left unused.

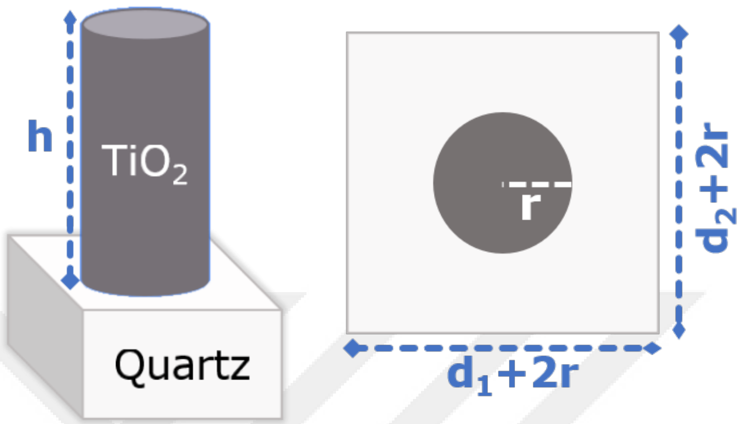

Figure 3.6: Cell representation used in ANSYS Lumerical FDTD Nanophotonics Simulator for the rectangular-stacked nanocylinders with $r = 45\,\mathrm{nm}$. Nanocylinder material (TiO_2) data is imported from [2], whereas substrate refractive index is taken from solver library. Constant d_2 of 30 nm is used. Adopted with permission from [1]. Copyright 2021 American Institute of Physics.

3.3 Triangular lattice stacking

While nanocylinders with continuously-tuned coupling in a single direction can serve well as metasurface phase elements, a generic geometry defined with arbitrary r, d_1, d_2 does not guarantee polarization-independent operation. The rectangular lattice does not have the same dispersion management capabilities along both orthogonal directions as orthogonal-coupling and parallel-coupling cases provide different levels. Starting from square packing and elongating it to acquire rectangular packing, the polarization degeneracy in the guided modes breaks down and the structure becomes birefringent as coupling asymmetry splits the modes. While an isotropic design can be constructed from anisotropic scatterers placed in a 4-fold symmetric manner, coupling to two modes with non-degenerate effective indices will result in undesired effects such as multi-mode propagation and inefficiency. On the surface, by choosing $d_1 = d_2$, an isotropic response is

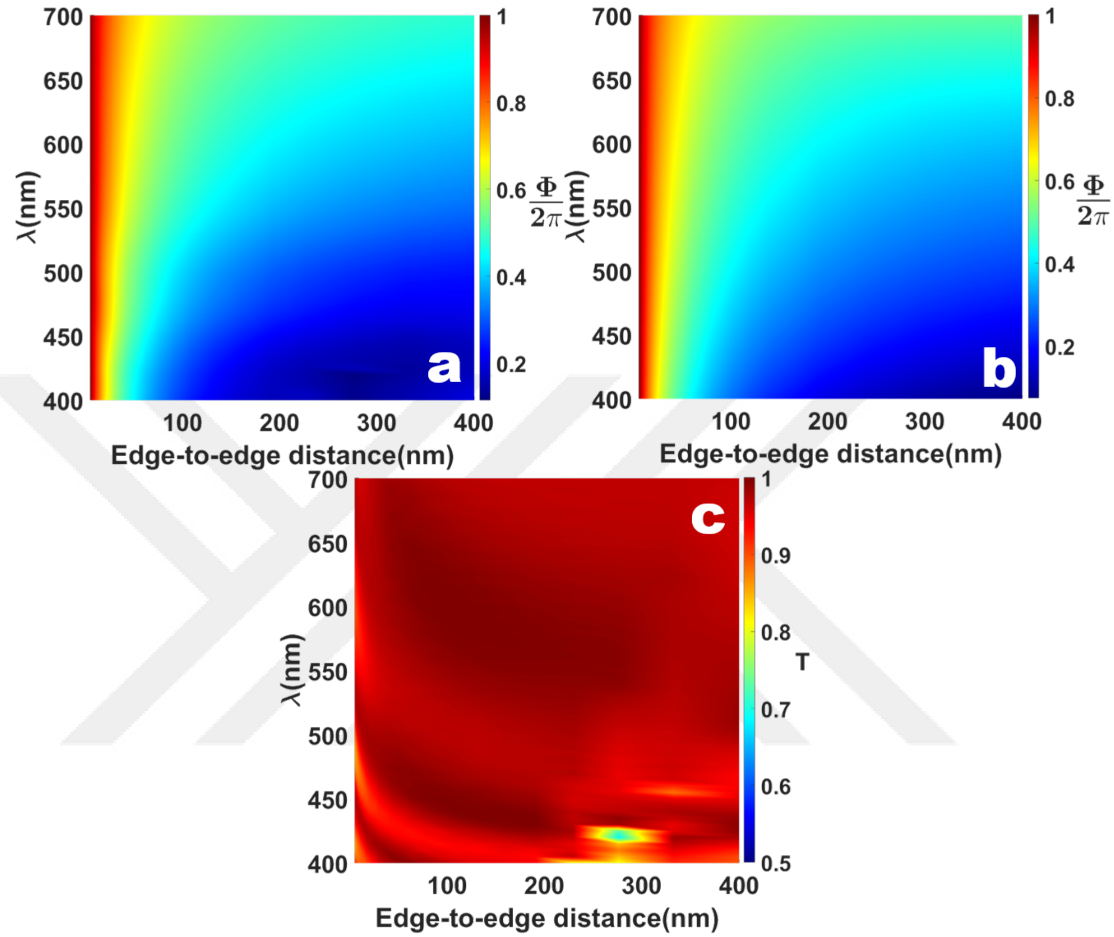

Figure 3.7: **a** Phase response of nanocylinders, referenced to uncoupled case. **b** Phase response acquired from Figure 3.5(b) as a result of propagation through $\Delta h = 600\,\text{nm}$. **c** Transmittance of the nanocylinders. The dip is potentially caused by a resonance. Adopted with permission from [1]. Copyright 2021 American Institute of Physics.

forced on the scatterer and polarization challenge can be resolved. However, as explained before, tiling of arbitrary squares is a completely different problem and is out of scope for this thesis.

While birefringence is crucial for components such as optical retarders, it is not a desirable feature for efficient focusing as unpolarized excitation will suffer from a functional efficiency viewpoint. To combat this, we can also stack the nanocylinders in a honeycomb lattice. The honeycomb lattice of nanocylinders is not 4-fold symmetric, but its response approaches circular symmetry as the characteristic lengths shrink. Also, as there are more neighboring elements in the designed cell interacting together, stacking is less sensitive to placement errors which are bound to occur. The field distributions for orthogonal polarizations are shown in Figure 3.8. As the lattice is 6-fold symmetric, $\hat{x}$-polarized excitation represents the best-coupled case, whereas $\hat{y}$-polarized excitation is coupled the least. Comparing Figure 3.8(a) and (b), we confirm that the response is almost identical in both cases.

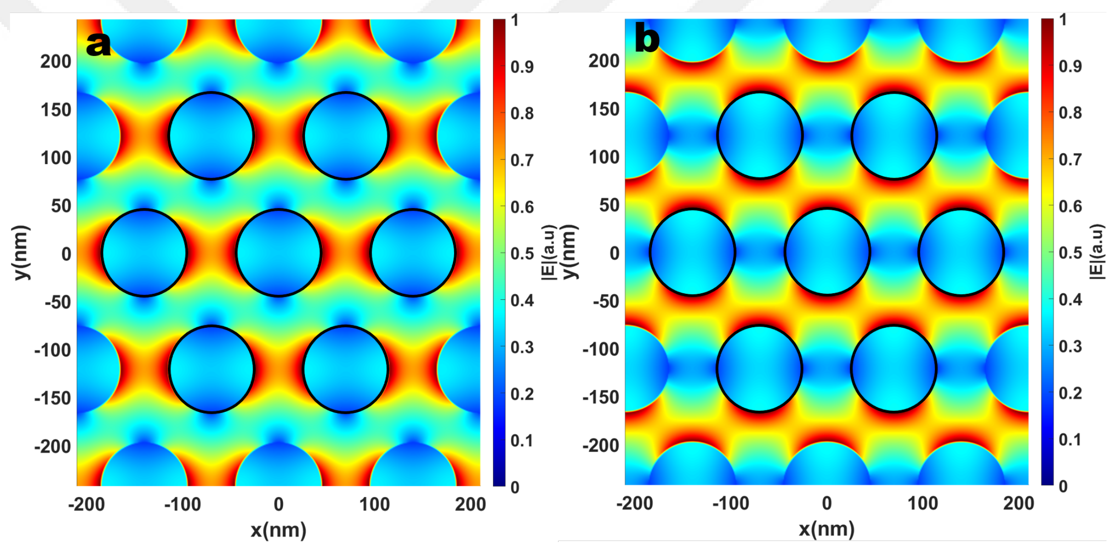

Figure 3.8: Electric field distributions for coupled circular waveguides in triangular lattice. $d = 50\,\text{nm}, \lambda = 400\,\text{nm}$. **a** $\hat{x}$-polarized and **b** $\hat{y}$-polarized. Adopted with permission from [1]. Copyright 2021 American Institute of Physics.

3.3.1 Waveguide simulations

Waveguide simulations were undertaken similar to the way described in Section 3.2.1. We also simulated for orthogonal polarizations and recorded the effective index difference maps across polarizations. In Figure 3.9 (a), we see the differential effective index map of honeycomb-stacked coupled waveguides across the whole visible range as the coupling distance d varies from 5 to 400 nm. The reference is taken as the uncoupled case. Generated Δn_{eff} is almost achromatic, with minor discrepancy in the long-wavelength limit. Simulations for orthogonal-polarized excitations were conducted, however, the differences between two cases were not distinguishable in linear scale. In Figure 3.9(b), the maximal effective index differences were plotted in logarithmic scale against the coupling distance d. Instead of the difference between effective index differentials, the absolute differences between the effective indices were calculated; since the latter also shows birefringence if exists. The case of $n_{eff,x} \neq n_{eff,y}$ and $\Delta n_{eff,x} \approx \Delta n_{eff,y}$ still generates achromatic functionality, but over a birefringent nature. This would have been analogous to a polarization-independent optical component, immediately followed by plain birefringent crystal, and the polarization state would not have been conserved. Hence, Figure 3.9 shows that our phase generation scheme is achromatic and conserves polarization states.

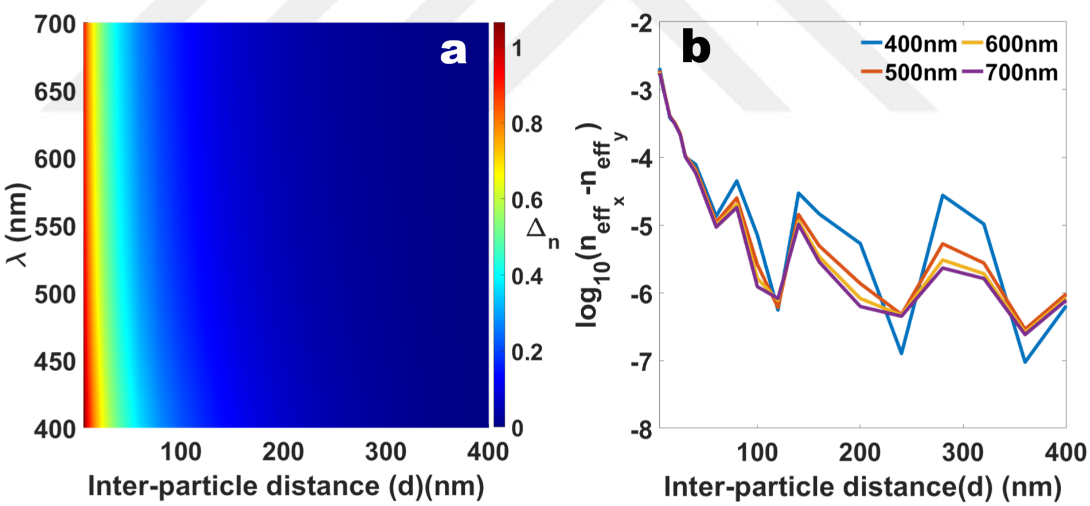

Figure 3.9: **a** Effective index difference map versus d and λ for coupled circular waveguides in triangular lattice, $\hat{x}$-polarized excitation. **b** Maximum absolute effective index difference between $\hat{x}$-polarized excitation and $\hat{y}$-polarized excitation. Adopted with permission from [1]. Copyright 2021 American Institute of Physics.

3.3.2 Confirmation with full electromagnetic solutions

A procedure similar to that of Section 3.2.2 is used for validation of the waveguiding approach and the extent of coupling. The response of the cells were simulated over the whole 400-700 nm range, with periodic boundary conditions in $\hat{x}, \hat{y}$ boundaries and PML boundary conditions in $\hat{z}$. Again, the substrate was chosen as quartz, and Palik's quartz refractive index data was used from the solver library. A broadband plane wave excitation with propagation direction along $+\hat{z}$ was injected within substrate. With the help of a field monitor placed 50 nm above the top end of the nanocylinders, the response was captured. Fields on the near-field monitor were then projected to far-field ($z = 10\,\mu\text{m}, x = y = 0$) via *farfieldexact3d* function in Lumerical library and propagation phase in the substrate and air were subtracted from the phase of the projected wave. With the remaining phase giving the phase response of the nanocylinders and the transmission from the monitor giving the transmittance of the nanocylinder, the results of these simulations are shown in Figure 3.10. The phase differential versus λ and d is presented in Figure 3.10(a). This result is compared with the waveguiding phase, calculated via $\Phi(d, \lambda, \Delta h) = 2\pi n_{eff}(d, \lambda)\dfrac{\Delta h}{\lambda}$, where $n_{eff}(d, \lambda)$ taken from Figure 3.9(b). A smaller portion of the phase maps are shown to increase the visibility of the similarities. The transmittance of the nanocylinder array is displayed in Figure 3.9(c). Unlike the rectangular case, the transmittance map is devoid of resonances, which is desired.

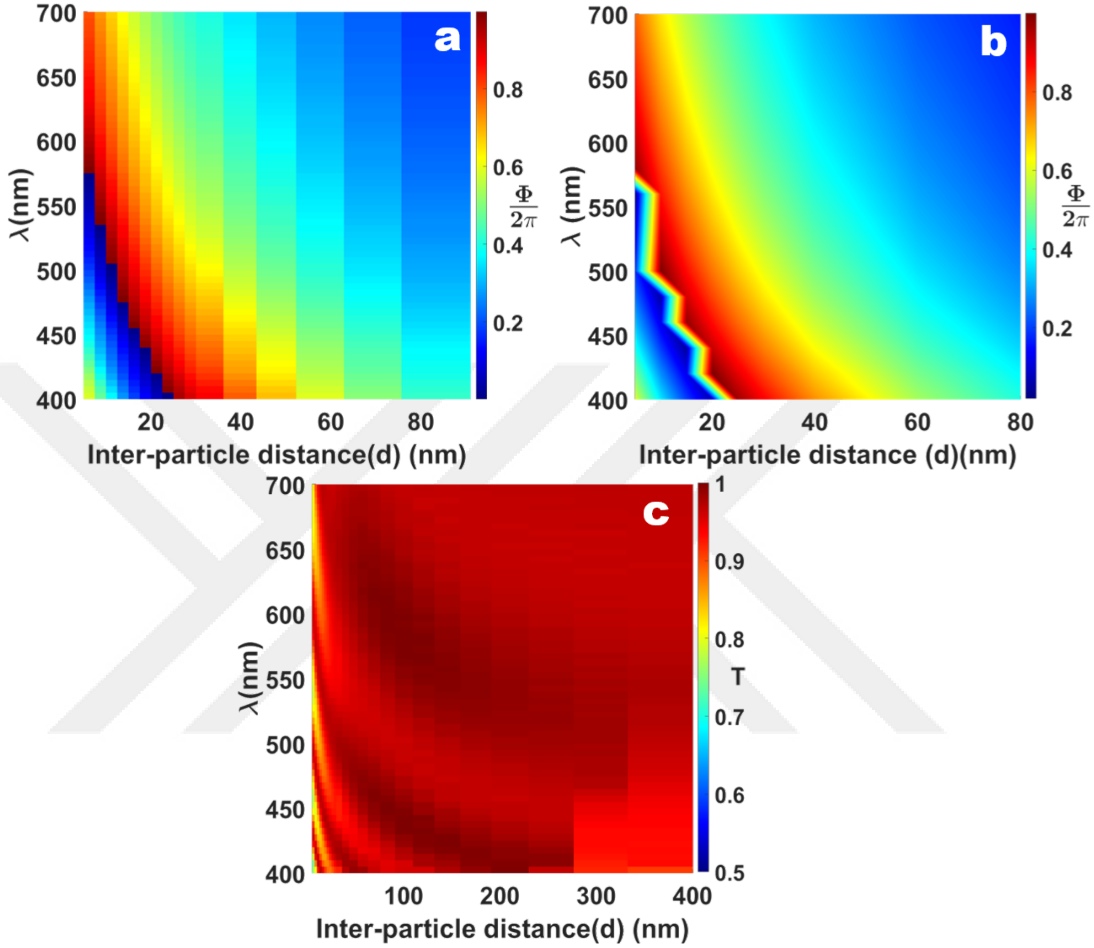

Figure 3.10: **a** Phase response of triangular stack of nanocylinders, referenced to uncoupled case. **b** Phase response acquired from Figure 3.9(a) as a result of propagation through $\Delta h = 600\,\text{nm}$. **c** Transmittance of the nanocylinders. Adopted with permission from [1]. Copyright 2021 American Institute of Physics.

3.4 Achromatic cylindrical metalens in visible region

To prove the validity of our approach, we designed a proof-of-concept achromatic cylindrical metalens from our rectangular-stacked coupled waveguides, working between $400 - 700$ nm. The phase function required for a lens is

$$\Phi(r, \lambda) = -\frac{2\pi}{\lambda}\left(\sqrt{r^2 + f^2} - f\right) \tag{3.2}$$

We can also express this phase in terms of phase accumulation via waveguiding:

$$\Phi(r, \lambda) = 2\pi\Delta n_{eff}(d_1, \lambda)\frac{\Delta h}{\lambda} \tag{3.3}$$

where $\Delta h = 600$ nm. From Figure 3.5(b), we see that $\Delta n_{eff} \approx \Delta n_{eff}(d_1)$ for the region of interest. Equating (3.2) and (3.3), we obtain

$$\frac{f - \sqrt{r^2 + f^2}}{\Delta h} = \Delta n_{eff}(d_1) \tag{3.4}$$

Let r_n denote the center position of the nth nanocylinder. Denoting center nanocylinder with index 0 ($r_0 = 0$), the additional nanocylinders are placed sequentially for all n, following the steps of

1. Look for the optimal spacing d in phase map given in Figure 3.7(a) such that $\Phi(d) = \frac{2\pi}{\lambda}\left(\sqrt{(r_{n-1} + d)^2 + f^2} - f\right)$
2. Place the nth cylinder and increment n.

We designed our lens to have a focal length of $f = 32$ µm with a numerical aperture (N.A.) of 0.154. The resulting metalens structure and its phase profile can be seen in Figures 3.11 and 3.12.

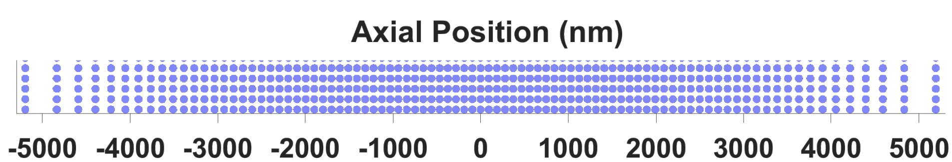

Figure 3.11: Generated layout of our achromatic cylindrical metalens with $f = 32$ µm and N.A.$= 0.154$. Adopted with permission from [1]. Copyright 2021 American Institute of Physics.

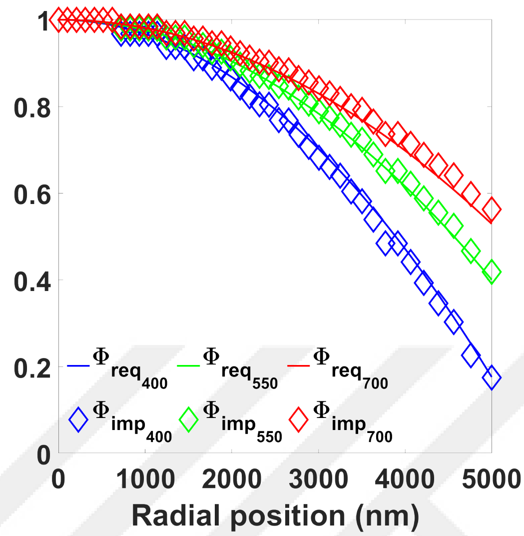

Figure 3.12: Required and actuated phase profiles for our achromatic cylindrical metalens with the layout given in Figure 3.11. Adopted with permission from [1]. Copyright 2021 American Institute of Physics.

We simulated our proof-of-concept designs in ANSYS Lumerical FDTD Nanophotonic Simulator. A broadband excitation, polarized along $\hat{x}$ and propagating along $+\hat{z}$ was injected from the quartz substrate. The metalens was meshed with constant grid of $dx = dy = 2\,\text{nm}$ and $dz = 10\,\text{nm}$. Instead of using far-field projection on the near-field field data acquired from a nearby monitor, we placed monitors along the propagation direction, which will record the wave getting focused and de-focused. This also enabled the use of multi-core computing on the data, as the solver computations can be parallelized whereas far-field computations could not.

Broadband functionality of a lens can be evaluated from the wavelength dependency of two characteristics: focusing efficiency and focusing distance. Additionally, for evaluation of non-chromatic aberrations, Strehl ratio, defined by the similarity between the theoretical diffraction pattern and measured intensity profile at the focal plane, is a widely-used figure of merit. We define Strehl ratio formally as:

$$SR(\lambda) = \frac{\int_A I_{meas}(r, z = f, \lambda)\, dA}{\int_A I_{aperture}(r, z = f, \lambda)\, dA} \tag{3.5}$$

Roughly, Strehl ratio translates to the maxima of the measured diffraction pattern, with total measured intensity normalized to total theoretical intensity. For diffraction-limited ideal focusing, $SR = 1$ - as the resolution drops, the pattern widens and the maximum point decreases.

For a cylindrical geometry, the aperture diffraction results in sinc^2 intensity dependence. Spot size is defined as the full-width-half-maximum (FWHM) of the intensity profile, and the diffraction limit is calculated from FWHM of the point-spread function of ideally diffracted wavefront of a slit aperture ($0.5\frac{NA}{\lambda}$). We define the focusing efficiency as the ability of the metalens to focus one unit of optical input, corresponding to transmittance of the metalens multiplied by relative focusing efficiency ($\int_{FWHM} I_{meas}\, dA)/(\int_{\infty} I_{meas}\, dA$).

Our achromatic cylinder metalens achieves 86% absolute focusing efficiency with 0.73 Strehl ratio and a spot size of 1.05 times the diffraction limit at the center wavelength. The broadband performance of our cylindrical metalens design is shown in Figure 3.13. In panel (a), the shift of the focal length with wavelength is displayed. The focal length changes between 28-33 µm, shortening as the wavelength becomes smaller, with the achromatic nature of the phase elements breaking down in this limit. Taking a look at Figure 3.12, we notice the small but persistent phase mismatch for $\lambda = 400\,\text{nm}$, causing higher phase differentials, larger optical curvature and subsequently shorter focal length. The diffractive performance across the spectrum can be seen from Figure 3.14. The non-uniform spot size can be corrected by choosing a different focal plane favoring the longer wavelengths, as the depth of focus for the metalens is long for the whole spectrum and a uniform-resolution point can be chosen without significant cost.

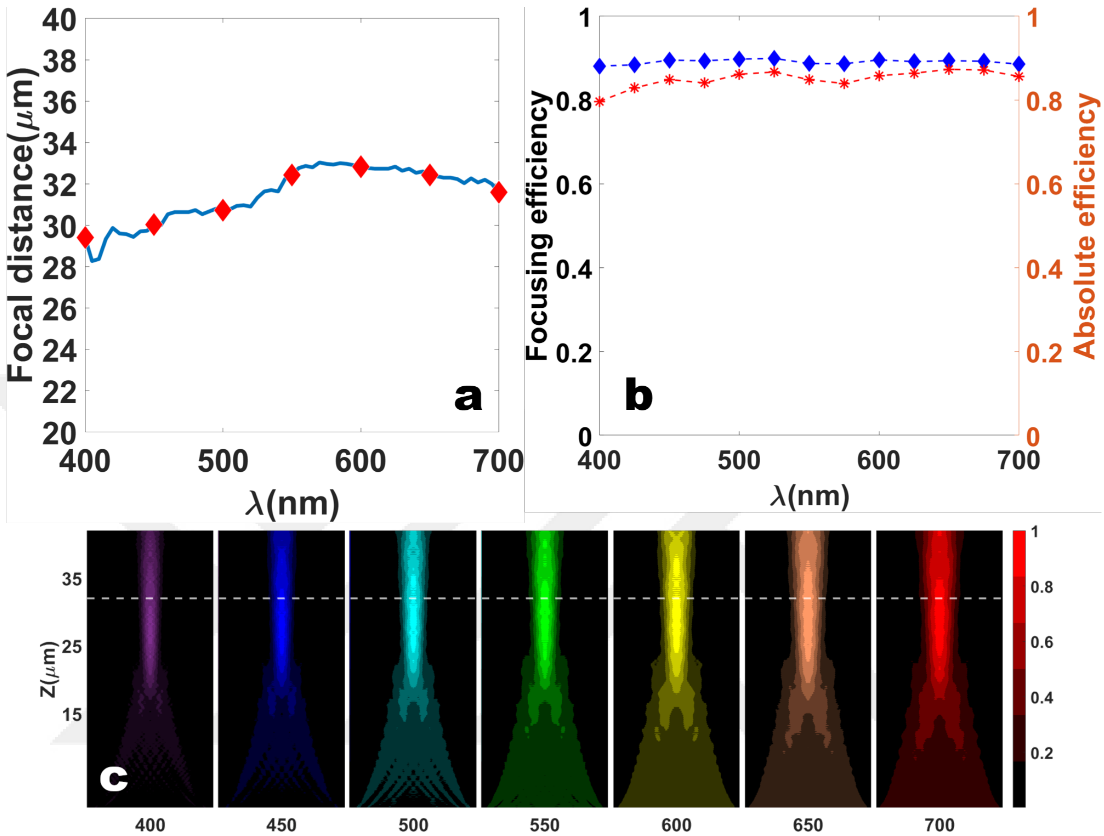

Figure 3.13: **a** Focal length versus wavelength for our cylindrical lens. Focal length shifts between 28-33 µm. **b** Absolute and relative focusing efficiencies versus wavelength. **c** False-colored intensity profiles along xz- plane. White dashed line represent the design focal length of 32 µm. Adopted with permission from [1]. Copyright 2021 American Institute of Physics.

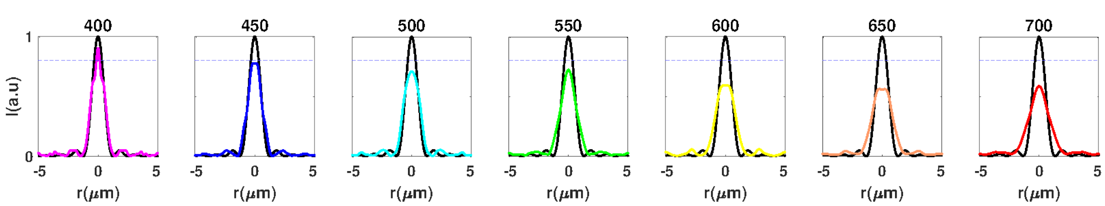

Figure 3.14: Intensity profiles at the focal planes for different wavelengths, normalized to ideal diffraction pattern with respect to total power. Dashed line corresponds to Strehl ratio of 0.8, commonly taken as the limit of aberration-free focusing. Adopted with permission from [1]. Copyright 2021 American Institute of Physics.

3.5 Achromatic and polarization-insensitive circular metalens in visible region

With the achromaticity condition satisfied with near-unity transmittance, one can design an achromatic and polarization-insensitive metalens. However, the tiling of the space still needs to be resolved. It is not possible to generate a triangular lattice with continuously changing element spacing. However, we can at least approximate it. High packing density of the triangular lattice is beneficial to this end as the packing errors will be distributed over a larger "permittivity mass". To overcome non-uniformities in inter-particle distances, placing of the nanopillars was carried out with the help of an optimization algorithm we devised for this purpose. Concentric circles of nanopillars, formed with respect to the phase requirements, were rotated iteratively, until the minimum point for the placement error is achieved. The mean squared error between the design and requirement was used as the cost function for optimization. The implementation details of the algorithm is described below.

1. Based on the relation between the phase difference and the edge-to-edge gap shown in Figure 3.10(a), a straight line of pillars, starting from the radial distance $r = 0$ to $r = R_{lens} = D_{lens}/2$ is constructed similar to our cylindrical lens placement, where R_{lens} is the maximum radial extent of the lens. Pillars after this initial placement, which are placed at $r = R_n$, are referenced as seed pillars (P_n).

2. For each pillar P_n, a concentric circle of pillars C_n is constructed based on the edge-to-edge distance required at $r = R_n$. Number of pillars on each concentric circle is found as such: For two pillars with edge-to-edge separation d_n, sitting on a concentric circle with radius R_n, the apex angle θ_n is calculated with $\theta_n = 2\sin^{-1}\left(\frac{d_n}{2R_n}\right)$. Number of pillars on the specified concentric circle $\#_n$ is then found via rounding $2\pi/\theta_n$ to the nearest integer. The edge-to-edge distance error found by this placement method has two contributions: a minor error from the rounding while finding $\#_n$ (error from

pillars in C_n), and a relatively large one from the other neighboring pillars (error from C_{n-1} and C_{n+1}).

3. For each C_n, relative distances of the constituting pillars is periodic with the corresponding θ_n. Calling the pillars in each C_n with their placement order, starting from $P_n = C_{n_1}$ until $C_{n_{\#n}}$, the average of edge-to-edge distances for six nearest neighbors for a given C_{n_m} has contributions from C_{n-1_p}, C_{n+1_q}, $C_{n_{m-1}}$ and $C_{n_{m+1}}$. After applying a rotation of $\phi = \theta_n$ to all the elements of C_n, either $C_{n_{m-1}}$ or $C_{n_{m+1}}$ will replace C_{n_m} and the rotated setup will be identical to the original setup. Therefore, we can argue that the optimization problem is at most N-dimensional, where N is the number of concentric circles. For N concentric circles, we utilized a generic particle swarm algorithm in Optimization Toolbox in MATLAB and took the rotation angles ϕ_n for each C_n as independent parameters, all in their respective $[0, \theta_N]$ range. The cost function for the optimization can then be found as follows: For each pillar in C_n, the average neighbor distance is computed by determining the 6 closest neighbors and taking their average. The relative error with respect to the expected edge-to-edge distances ϵ_{n_m} is found for all pillars in C_n, then an average error for C_n is obtained by $\epsilon_n = \frac{1}{\#_n} \sum_m \epsilon_{n_m}$.The cost function is finally taken as $\max(\epsilon_n)$.

For the convergence of the algorithm, the phase map should be continuous throughout the design. The scalability property of the waveguide phase provides a solution to this problem. For designs with larger absolute phase coverage, the design height can be scaled up so that the phase coverage is continuous.

Next, as a proof of our concept, we generated an achromatic and polarization-insensitive circular lens with $f = 11\,\mu\text{m}$ and N.A. of 0.26 via the described placement algorithm. The utilization of placement algorithm reduced the placement errors in the initial design, bringing down the average marginal error from 22% to 6%. The final design for achromatic and polarization-insensitive metalens is shown in Figure 3.16.

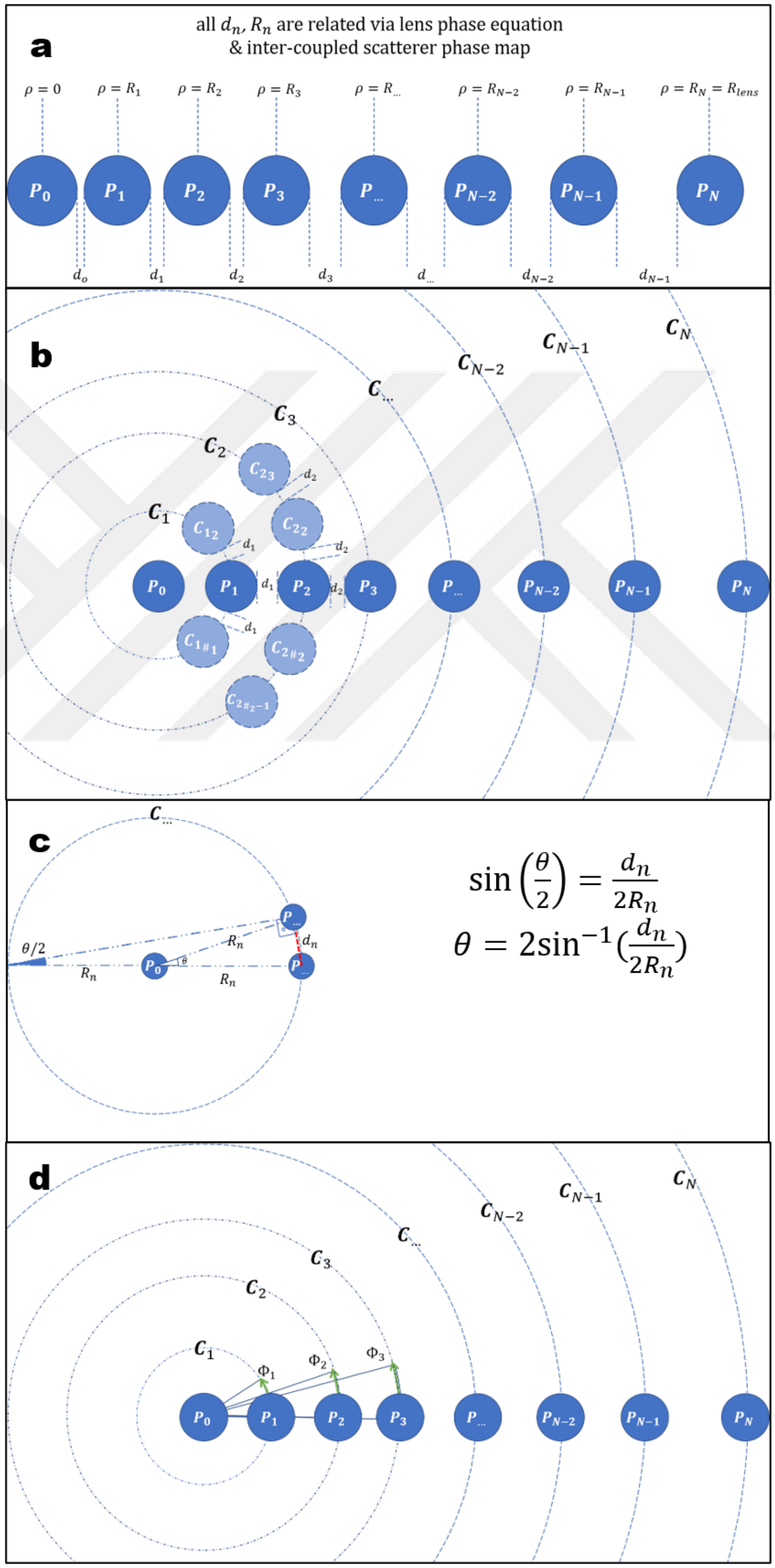

Figure 3.15: Steps of our deterministic placement algorithm described in Section 3.5. Adopted with permission from [1]. Copyright 2021 American Institute of Physics.

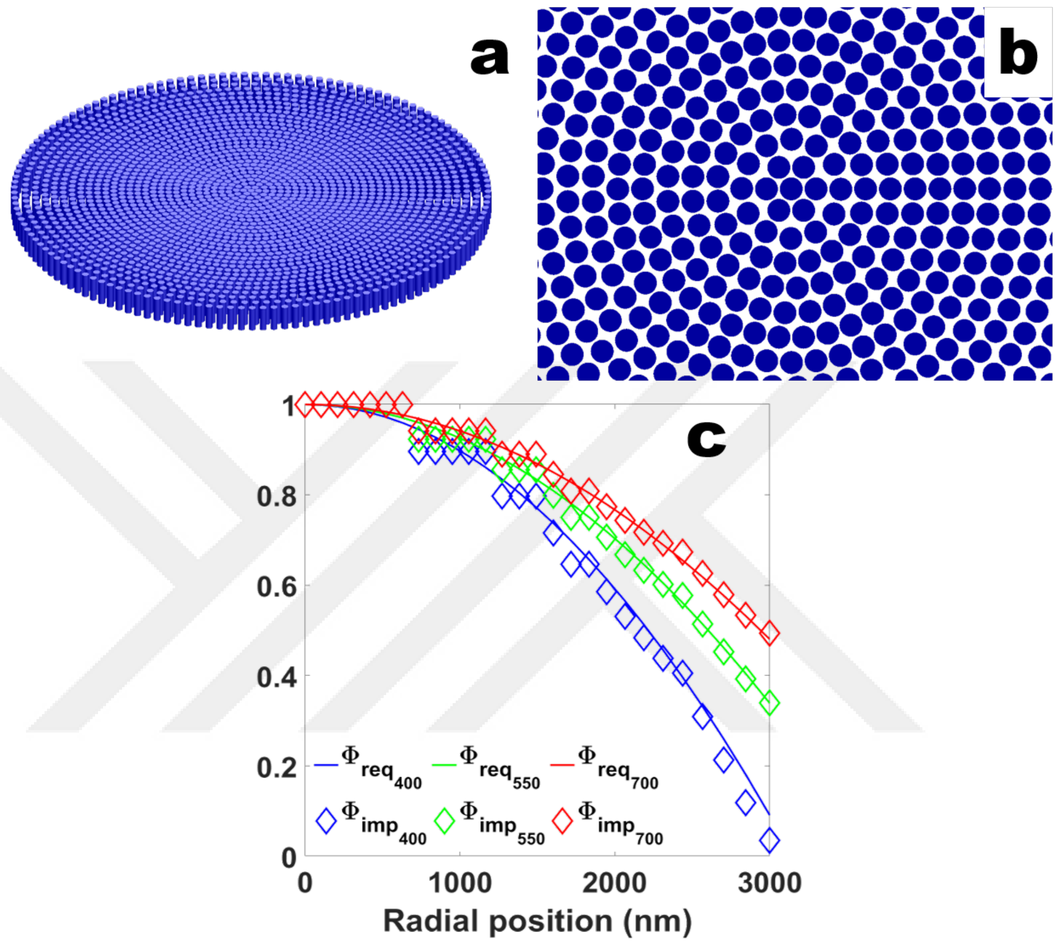

Figure 3.16: **a** Generated layout of achromatic circular metalens with $f = 11\,\mu\text{m}$ and N.A.= 0.26. **b** Detailed bird's eye view for the central region of the design. **c** Required and actuated phase profiles for our achromatic circular lens with the layout given in (a-b). Adopted with permission from [1]. Copyright 2021 American Institute of Physics.

We simulated our proof-of-concept designs in ANSYS Lumerical FDTD Nanophotonic Simulator. Initially, the metalens was tested under excitation with E-field along $\hat{x}$ and propagation direction along $+\hat{z}$, injected from the quartz substrate. The metalens was meshed with a constant grid of $dx = dy = 2\,\text{nm}$ and $dz = 10\,\text{nm}$. The same simulations were repeated with the polarization of the excitation aligned with $\hat{y}$, and the results were compared.

The same figure-of-merit definitions defined in Section 3.4, namely absolute focusing efficiency, focal shift for broadband performance and Strehl ratio for resolution, were computed. For the calculations regarding the ideal diffraction pattern, a circular aperture was used as a reference, resulting in a diffraction limit of $0.514\lambda/N.A.$ for the FWHM of the point-spread function of Airy disk (J_1^2 dependence).

The broadband performance of our circular metalens design is shown in Figure 3.17. Our achromatic cylinder metalens achieves 62% absolute focusing efficiency with 0.96 Strehl ratio and a spot size of 1.03 times the diffraction limit at the center wavelength. In Figure 3.17(a), the shift of the focal length with wavelength is displayed. Compared to our cylindrical lens design, our circular lens has superior achromaticity, due to the placement optimization algorithm presented in Section 3.5. The focal length changes between 10.5-11.2 µm, but it is similar in both polarizations. In Figure 3.17(b), we see the functional efficiency versus λ for both polarizations. The maximum absolute focusing efficiency difference between polarizations is 3%. These results set the record for efficiencies in broadband designs in the visible region with polarization-independent operation and insignificant focal shift, to the best of our knowledge. In the top half of Figure 3.17(c), false-colored intensity profile along xz-plane is displayed, whereas bottom half shows the superb resolution of our metalens with a maximum Strehl ratio of 0.96 and minimum of 0.8. At the center wavelength, these correspond to spot sizes of 1.03 times the diffraction limit.

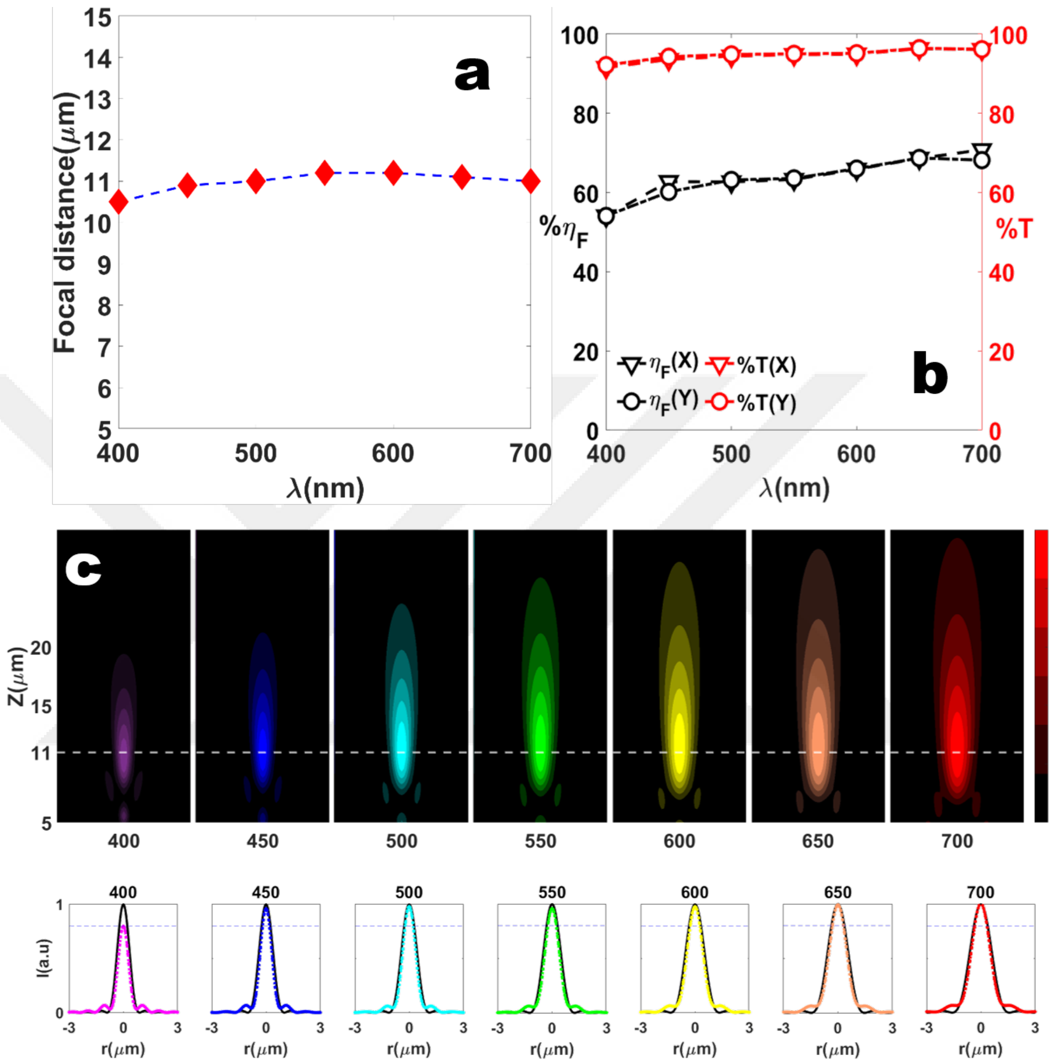

Figure 3.17: **a** Focal length versus wavelength for our circular lens. Focal length shifts between 10.5-11.2 µm. **b** Absolute focusing efficiency and total transmittance versus wavelength. Instead of relative focusing efficiency, transmittance is used to enhance the visibility. **c** Top: False-colored intensity profiles along xz-plane versus λ. White dashed line represents the design focal length of 11 µm. Bottom: Intensity profiles at the focal plane versus λ, normalized to ideal diffraction pattern with respect to total power. Dashed line corresponds to Strehl ratio of 0.8. Adopted with permission from [1]. Copyright 2021 American Institute of Physics.

Table 3.1: Performance metrics of previously reported achromatic metalenses and their comparison to our cylindrical and circular MAM lenses presented in this thesis, which are comprised of the proposed cell-less phase elements with waveguide-coupling approach. Adopted with permission from [1]. Copyright 2021 American Institute of Physics.

	$\frac{\text{FWHM spot size}(f_{center})}{\text{Diffraction limit}(f_{center})}$	Strehl ratio	$\eta_{abs}(f_{center})$	Polarization	$\frac{\Delta f}{f_{center}}$	N.A.
Reference [13][a]	$\sim$ 1.35 µm/1.35 µm	~90%	~20%	Circular	190 THz/525 THz	0.2
Reference [14][a]	$\sim$ 2.75 µm/2.5 µm	×	~50%	Circular	195 THz/565 THz	0.106
Reference [37][a]	$\sim$ 1.5 µm/1.46 µm	~80%	34%	Insensitive	225 THz/515 THz	0.2
Reference [38][a]	$\sim$ 800 nm/760 nm	N.A. too high	×	Insensitive	35 THz/230 THz	0.88
Reference [39][a]	$\sim$ 4.28 µm/4.28 µm	~85%	65%	Insensitive	218 THz/325 THz	0.12
This Thesis: Cylindrical MAM lens[b]	1.87 µm/1.78 µm	73%	86%	Linear	320 THz/545 THz	0.154
This Thesis: Circular MAM lens[b]	1.06 µm/1.03 µm	96%	62%	Insensitive	320 THz/545 THz	0.26

[a] Measurement
[b] Simulation
[×] Not available

In Table 3.1, we compare the performance of our designs with the best performance reports found in literature from the last two years. Our proposed cylindrical lens outperforms all the other designs in efficiency, whereas the circular lens is highly diffraction-limited, achromatic and has polarization-insensitive operation. Here, the high absolute efficiencies of our devices prove the effectiveness of our cell-less metasurface paradigm in wavefront manipulation.

3.6 Summary

In this chapter, we have demonstrated that our proposed continuously tuned fabric of inter-scatterer coupling can be utilized as an achromatic phase accumulation mechanism for geometries operating in guiding mode. This paradigm allowed us to devise metasurfaces that interact with the incoming wave much more effectively than metalenses of similar functionalities previously reported in the literature, all of which rely on uncoupled meta-cells. Based on our cell-less metasurface concept, we were able to show polarization-insensitive and efficient operation and achieve fully achromatic focusing in the entirety of the visible range. The findings here altogether indicate that continuously tuning the coupling of identical nanopillars in a two-dimensional lattice provides a highly effective approach to make efficient metasurfaces.

Chapter 4

Conclusion and future outlook

In this thesis work, we studied the effect of inter-waveguide coupling using waveguide simulations and full electromagnetic solutions. We showed that the utilization of the coupling between identical elements can be used for creating dispersionless phase generation schemes, producing what we call MAM fabrics, applicable to the generation of high-resolution, high-efficiency and broadband focusing in the visible region. We devised an optimization algorithm for creating 2-D fabrics of inter-coupled metastructures to achieve almost diffraction-limited focusing for arbitrarily polarized inputs. We designed and showed one cylindrical and one circular metalens operating in the visible region and validated its superior performance via comparing its figure-of-merits to the significant examples in the last two years in the literature. We used the commercial software package ANSYS Lumerical for full electromagnetic simulations (FDTD Nanophotonics Simulator) and waveguide simulations (MODE Waveguide Simulator), and Optimization Toolbox from MATLAB for devising our optimization algorithm.

Metasurfaces do not exist as numerical artifacts in the scientific world. A vast array of fabrication techniques are available for fabrication of sub-wavelength structures. These are driven with the advent of nanofabrication technologies, and there is a great incentive to adapt metastructures to the optimized methods of the silicon industry [40]. The general process flow for metasurfaces consist of sequential applications of patterning, development, deposition, lift-off and/or etching.

To realize the full potential of metasurface concept, designs need to be able to be scalable not only in $\hat{z}$, but also in the transverse plane. Large-area metasurface implementations are increasingly receiving attention, even in the visible range [41] - although large-scale achromatic lenses have not been achieved yet. Our MAM concept offers scalability as the waveguide phase linearly scales with the total height of the structure. However, due to strict requirement of coupling for phase generation, discontinuities in the required phase profile pose challenges in tiling. One approach is to increase the propagation distance to create a uniform distribution of phase across the whole transverse plane - decreasing the density of the fabric with increasing radial placement, and ending with uncoupled waveguides at the edges of the design. This methodology is identical with the fabrication of convex lenses with continuous surfaces. The required phase differential increases linearly with radial device size as $\sqrt{r_{max}^2 + f^2} - f \approx r_{max}$ for $r >> f$. This implies metastructure height also increasing linearly with radial size, effectively forming a macroscopic effective-index crystal. Thus, in the large scale, this approach ceases to be compact. However, in the intermediate region (sub-millimeter sizes), this approach is powerful when combined with high-resolution small-area patterning techniques such as electron-beam lithography and high-AR etching techniques such as metal-assisted chemical etching [42] and Bosch process, also known as deep reactive-ion etching [43]. Within this size bounds, MAM concept can be useful for creation of focal plane arrays, integrated with CMOS sensors.

Alternatively, one can adopt the approach of Fresnel lenses, and form discontinuities in the phase surfaces. This approach increases the applicability of MAM concept, but decreases the diffractive performance of the lens, as a consequence of the curvature of the phase front approaching a linear ramp as device size grows large. The phase jumps might be too rapid to form efficient fabrics. However, to overcome this challenge, an extension of the MAM concept can be applied to linear coupling between identical waveguides placed on a ring, isolated from the neighbors in the radial direction. This scheme approximates the rectangular stacking of nanopillars as the radius increases.

Here, we propose and describe a representative process flow for MAMs that is feasible on silicon as a future outlook. This process flow includes metal-assisted chemical etching, a wet etching technique utilizing spatial control of silicon oxidation with patterned metal films acting as catalysts. The substrate is considered to be as high-resistivity silicon.

The proposed fabrication steps follow:

1. The substrate is to be cleaned with RCA1/RCA2 standard cleaning procedures and then is spin-coated with high-resolution electron-beam resist. Two-step resist coating can be used to enhance the resolution of the patterns. To prevent charging effects in the substrate, a thin gold layer or conductive polymer can be deposited on the substrate prior to exposure as a conductive channel.

2. The negative of the generated MAM design is to be exposed by using electron-beam lithography. The conductive layer can be removed by dissolving the layer either in aqua regia (for gold) or in water (conductive polymer). The resist in the exposed regions (inter-waveguide gaps) are to be dissolved in a developer of choice. The parameters of the patterning are to be optimized; good control of development temperature or exposure dose and usage of pattern correction schemes are often required.

3. To act as a catalyst, a sufficiently thin film of gold is to be thermally evaporated on the sample. The film needs to be porous enough to achieve directional etching. The remaining resist patterns are to be lifted off, leaving patches of metal films at the location of inter-waveguide gaps.

4. The sample is to be put into a mixture of ethanol, isopropanol and hydrofluoric acid. The regions of silicon underneath the metal patches will become activated due to hole generation around the metal film and transform into silica, which is immediately dissolved in hydrofluoric acid. The metal film is expected to sink as the silicon underneath is being etched. To prevent change of etching direction, ferromagnetic films [44] or self-anchoring porous metal films [45] can be used.

5. After the waveguides are created with sufficient etching, the residual catalyst layer can be dissolved in aqua regia.

6. Finally, to form a protective layer and prevent spontaneous collapse of high-aspect-ratio cylinders, a silica layer is to be deposited with chemical vapor deposition.

For the steps involving chemical processing (development of electron-beam resist and silicon etching), these processes can be studied under varying thermal conditions or doping. With decreasing process temperatures and lighter doping, the activation and dissolution processes become slower but more accurate, enabling high-contrast surfaces.

The exemplary process flow we presented here can be modified for designs utilizing different waveguide materials, as long as the desired material is compatible with high-precision deposition techniques. This is possible by using silicon as a sacrificial layer, a layer that will be absent in the final design, but will be used as an intermediate mold. The required modifications may involve **(i)** exposure of the pillars, instead of the gaps in step 2, leaving catalyst patches at the waveguide locations following step 3 **(ii)** deposition of the desired material to the waveguide locations after step 5, followed by **(iii)** removal of sacrificial silicon layer by means of selective etching techniques, for example, XeF_2 etching.

The MAM concept is not limited to the visible range, or the choice of dielectric material. As long as the waveguide material is lossless and is operated in its Cauchy regime, cylinder radius a and coupling vector $\mathbf{d}$ can be chosen so that the coupling introduces anomalous dispersion, negating the material dispersion. The availability of high-index materials and reduction of resolution requirements in patterning and/or etching for longer wavelengths, especially near-infrared, is promising for MAM applications.

Bibliography

[1] H. B. Yağcı and H. V. Demir, "'Meta-atomless' architecture based on an irregular continuous fabric of coupling-tuned identical nanopillars enables highly efficient and achromatic metasurfaces," Applied Physics Letters, vol. 118, p. 081105, Feb. 2021.

[2] T. Siefke, S. Kroker, K. Pfeiffer, O. Puffky, K. Dietrich, D. Franta, I. Ohlídal, A. Szeghalmi, E.-B. Kley, and A. Tünnermann, "Materials pushing the application limits of wire grid polarizers further into the deep ultraviolet spectral range," Advanced Optical Materials, vol. 4, pp. 1780–1786, July 2016.

[3] M. Price, "You can thank your fruit-hunting ancestors for your color vision," Science, Feb. 2017.

[4] C. P. van den Berg, J. Troscianko, J. A. Endler, N. J. Marshall, and K. L. Cheney, "Quantitative colour pattern analysis (QCPA): A comprehensive framework for the analysis of colour patterns in nature," Methods in Ecology and Evolution, vol. 11, pp. 316–332, Dec. 2019.

[5] L. A. Isbell, "Snakes as agents of evolutionary change in primate brains," Journal of Human Evolution, vol. 51, pp. 1–35, July 2006.

[6] V. G. Veselago, "The electrodynamics of substances with simultaneously negative values of ϵ an μ," Soviet Physics Uspekhi, vol. 10, pp. 509–514, Apr 1968.

[7] J. B. Pendry, "Negative refraction makes a perfect lens," Phys. Rev. Lett., vol. 85, pp. 3966–3969, Oct 2000.

[8] D. Schurig, J. J. Mock, B. J. Justice, S. A. Cummer, J. B. Pendry, A. F. Starr, and D. R. Smith, "Metamaterial electromagnetic cloak at microwave frequencies," Science, vol. 314, no. 5801, pp. 977–980, 2006.

[9] X. Ni, N. K. Emani, A. V. Kildishev, A. Boltasseva, and V. M. Shalaev, "Broadband light bending with plasmonic nanoantennas," Science, vol. 335, pp. 427–427, Dec. 2011.

[10] A. Pors, M. G. Nielsen, R. L. Eriksen, and S. I. Bozhevolnyi, "Broadband focusing flat mirrors based on plasmonic gradient metasurfaces," Nano Letters, vol. 13, pp. 829–834, Jan. 2013.

[11] Y. Yao, R. Shankar, M. A. Kats, Y. Song, J. Kong, M. Loncar, and F. Capasso, "Electrically tunable metasurface perfect absorbers for ultrathin mid-infrared optical modulators," Nano Letters, vol. 14, pp. 6526–6532, Oct. 2014.

[12] M. Khorasaninejad, Z. Shi, A. Y. Zhu, W. T. Chen, V. Sanjeev, A. Zaidi, and F. Capasso, "Achromatic metalens over 60 nm bandwidth in the visible and metalens with reverse chromatic dispersion," Nano Letters, vol. 17, pp. 1819–1824, Feb. 2017.

[13] W. T. Chen, A. Y. Zhu, V. Sanjeev, M. Khorasaninejad, Z. Shi, E. Lee, and F. Capasso, "A broadband achromatic metalens for focusing and imaging in the visible," Nature Nanotechnology, vol. 13, pp. 220–226, Jan. 2018.

[14] S. Wang, P. C. Wu, V.-C. Su, Y.-C. Lai, M.-K. Chen, H. Y. Kuo, B. H. Chen, Y. H. Chen, T.-T. Huang, J.-H. Wang, R.-M. Lin, C.-H. Kuan, T. Li, Z. Wang, S. Zhu, and D. P. Tsai, "A broadband achromatic metalens in the visible," Nature Nanotechnology, vol. 13, pp. 227–232, Jan. 2018.

[15] J. A. Fan, "Freeform metasurface design based on topology optimization," MRS Bulletin, vol. 45, pp. 196–201, Mar. 2020.

[16] R. Paniagua-Domínguez, Y. F. Yu, E. Khaidarov, S. Choi, V. Leong, R. M. Bakker, X. Liang, Y. H. Fu, V. Valuckas, L. A. Krivitsky, and A. I. Kuznetsov, "A metalens with a near-unity numerical aperture," Nano Letters, vol. 18, pp. 2124–2132, Feb. 2018.

[17] G.-Y. Lee, J.-Y. Hong, S. Hwang, S. Moon, H. Kang, S. Jeon, H. Kim, J.-H. Jeong, and B. Lee, "Metasurface eyepiece for augmented reality," Nature Communications, vol. 9, Nov. 2018.

[18] M. Wu, S. T. Ha, S. Shendre, E. G. Durmusoglu, W.-K. Koh, D. R. Abujetas, J. A. Sánchez-Gil, R. Paniagua-Domínguez, H. V. Demir, and A. I. Kuznetsov, "Room-temperature lasing in colloidal nanoplatelets via mie-resonant bound states in the continuum," Nano Letters, vol. 20, pp. 6005–6011, June 2020.

[19] A. Leitis, A. Heßler, S. Wahl, M. Wuttig, T. Taubner, A. Tittl, and H. Altug, "All-dielectric programmable huygens' metasurfaces," Advanced Functional Materials, vol. 30, p. 1910259, Mar. 2020.

[20] H. Sroor, Y.-W. Huang, B. Sephton, D. Naidoo, A. Vallés, V. Ginis, C.-W. Qiu, A. Ambrosio, F. Capasso, and A. Forbes, "High-purity orbital angular momentum states from a visible metasurface laser," Nature Photonics, vol. 14, pp. 498–503, Apr. 2020.

[21] T. X. Hoang, S. T. Ha, Z. Pan, W. K. Phua, R. Paniagua-Domínguez, C. E. Png, H.-S. Chu, and A. I. Kuznetsov, "Collective mie resonances for directional on-chip nanolasers," Nano Letters, vol. 20, pp. 5655–5661, June 2020.

[22] D. Pozar, "Wideband reflectarrays using artificial impedance surfaces," Electronics Letters, vol. 43, no. 3, p. 148, 2007.

[23] A. Niv, G. Biener, V. Kleiner, and E. Hasman, "Propagation-invariant vectorial bessel beams obtained by use of quantized pancharatnam–berry phase optical elements," Optics Letters, vol. 29, p. 238, Feb. 2004.

[24] E. Karimi, S. A. Schulz, I. D. Leon, H. Qassim, J. Upham, and R. W. Boyd, "Generating optical orbital angular momentum at visible wavelengths using a plasmonic metasurface," Light: Science & Applications, vol. 3, pp. e167–e167, May 2014.

[25] N. Yu, P. Genevet, M. A. Kats, F. Aieta, J.-P. Tetienne, F. Capasso, and Z. Gaburro, "Light propagation with phase discontinuities: Generalized laws of reflection and refraction," Science, vol. 334, pp. 333–337, Sept. 2011.

[26] O. Akın and H. V. Demir, "Mid-wave infrared metasurface microlensed focal plane array for optical crosstalk suppression," Optics Express, vol. 23, p. 27020, Oct. 2015.

[27] O. Akın and H. V. Demir, "High-efficiency low-crosstalk dielectric metasurfaces of mid-wave infrared focal plane arrays," Applied Physics Letters, vol. 110, p. 143106, Apr. 2017.

[28] L. Wang, S. Kruk, H. Tang, T. Li, I. Kravchenko, D. N. Neshev, and Y. S. Kivshar, "Grayscale transparent metasurface holograms," Optica, vol. 3, p. 1504, Dec. 2016.

[29] İbrahim Tanriover and H. V. Demir, "Broad-band polarization-insensitive all-dielectric metalens enabled by intentional off-resonance waveguiding at mid-wave infrared," Applied Physics Letters, vol. 114, p. 043105, Jan. 2019.

[30] I. Tanrıöver, Universally polarization-insensitive achromatic metasurfaces. MS Thesis, Bilkent University, 2019.

[31] D. Marcuse, Light Transmission Optics. Bell Laboratories series, Van Nostrand Reinhold, 1982.

[32] L. Zhang, Q. Lin, Y. Yue, Y. Yan, R. G. Beausoleil, and A. E. Willner, "Silicon waveguide with four zero-dispersion wavelengths and its application in on-chip octave-spanning supercontinuum generation," Optics Express, vol. 20, p. 1685, Jan. 2012.

[33] Y. Bidaux, F. Kapsalidis, P. Jouy, M. Beck, and J. Faist, "Coupled-waveguides for dispersion compensation in semiconductor lasers," Laser & Photonics Reviews, vol. 12, p. 1700323, Mar. 2018.

[34] V. R. Almeida, Q. Xu, C. A. Barrios, and M. Lipson, "Guiding and confining light in void nanostructure," Optics Letters, vol. 29, p. 1209, June 2004.

[35] W. Gambling, H. Matsumura, and C. Ragdale, "Mode dispersion, material dispersion and profile dispersion in graded-index single-mode fibres," IEE Journal on Microwaves, Optics and Acoustics, vol. 3, no. 6, p. 239, 1979.

[36] J. Cannon, W. Floyd, and W. Parry, Squaring rectangles: the finite Riemann mapping theorem. Geometry Center: Research report GCG, 1993.

[37] W. T. Chen, A. Y. Zhu, J. Sisler, Z. Bharwani, and F. Capasso, “A broadband achromatic polarization-insensitive metalens consisting of anisotropic nanostructures,” Nature Communications, vol. 10, Jan. 2019.

[38] S. Shrestha, A. C. Overvig, M. Lu, A. Stein, and N. Yu, “Broadband achromatic dielectric metalenses,” Light: Science & Applications, vol. 7, Nov. 2018.

[39] A. Ndao, L. Hsu, J. Ha, J.-H. Park, C. Chang-Hasnain, and B. Kanté, “Octave bandwidth photonic fishnet-achromatic-metalens,” Nature Communications, vol. 11, June 2020.

[40] “Metalenz reimagines the camera in 2D and raises $10M to ship it.”

[41] J.-S. Park, S. Zhang, A. She, W. T. Chen, P. Lin, K. M. A. Yousef, J.-X. Cheng, and F. Capasso, “All-glass, large metalens at visible wavelength using deep-ultraviolet projection lithography,” Nano Letters, vol. 19, pp. 8673–8682, Nov. 2019.

[42] L. Romano, M. Kagias, J. Vila-Comamala, K. Jefimovs, L.-T. Tseng, V. A. Guzenko, and M. Stampanoni, “Metal assisted chemical etching of silicon in the gas phase: a nanofabrication platform for x-ray optics,” Nanoscale Horizons, vol. 5, no. 5, pp. 869–879, 2020.

[43] N. Chekurov, K. Grigoras, A. Peltonen, S. Franssila, and I. Tittonen, “The fabrication of silicon nanostructures by local gallium implantation and cryogenic deep reactive ion etching,” Nanotechnology, vol. 20, p. 065307, Jan. 2009.

[44] K. Balasundaram, P. K. Mohseni, Y.-C. Shuai, D. Zhao, W. Zhou, and X. Li, “Photonic crystal membrane reflectors by magnetic field-guided metal-assisted chemical etching,” Applied Physics Letters, vol. 103, p. 214103, Nov. 2013.

[45] J. D. Kim, M. Kim, L. Kong, P. K. Mohseni, S. Ranganathan, J. Pachamuthu, W. K. Chim, S. Y. Chiam, J. J. Coleman, and X. Li, "Self-anchored catalyst interface enables ordered via array formation from submicrometer to millimeter scale for polycrystalline and single-crystalline silicon," ACS Applied Materials & Interfaces, vol. 10, no. 10, pp. 9116–9122, 2018. PMID: 29406759.